
Faculty of Science

Faculty Publications

This is a post-print version of the following article:

Uncovering the nature of electroactive sites in nano architected dendritic Bi for highly efficient CO₂ electroreduction to formate

Mengyan Fan, Sagar Prabhudev, Sébastien Garbarino, Jinli Qiao, Gianluigi A. Botton, David A. Harrington, Ana C. Tavares, and Daniel Guay

2020

The final publication is available at:

<https://doi.org/10.1016/j.apcatb.2020.119031>

Citation for this paper:

Fan, M., Prabhudev, S., Garbarino, S., Qiao, J., Botton, G. A., Harrington, D. A., Tavares, A. C., & Guay, D. (2020). Uncovering the nature of electroactive sites in nano architected dendritic Bi for highly efficient CO₂ electroreduction to formate. *Applied Catalysis B: Environmental*, 274(2020). <https://doi.org/10.1016/j.apcatb.2020.119031>

© 2020. This manuscript version is made available under the CC-BY-NC-ND 4.0 license
<http://creativecommons.org/licenses/by-nc-nd/4.0/>

Uncovering the Nature of Electroactive Sites in Nano Architected Dendritic Bi for Highly Efficient CO₂ Electroreduction to Formate

Mengyang Fan,¹ Sagar Prabhudev,^{1,2} Sébastien Garbarino,³ Jinli Qiao,⁴
Gianluigi A. Botton,² David A. Harrington,⁵ Ana C. Tavares¹ and Daniel Guay^{1*}

¹ INRS-Énergie, Matériaux Télécommunications
1650 Lionel-Boulet Boulevard, P. O. Box 1020,
Varenes, QC, Canada J3X 1S2

² McMaster University, Brockhouse Institute for Materials Research and Canadian Centre
for Electron Microscopy
1280 Main Street West,
Hamilton, ON, Canada L8S 4M1

³ PRIMA Québec
505 Boulevard Maisonneuve Ouest,
Montréal, QC, Canada H3A 3C2

⁴ State Environmental Protection Engineering Center for Pollution
Treatment and Control in Textile Industry,
College of Environmental Science and Engineering, Donghua University
2999 Ren'min North Road,
Shanghai, PR China 201620

⁵ Department of Chemistry, University of Victoria
3800 Finnerty Rd, P. O. Box 1700,
Victoria, BC, Canada V8W 2Y2

* Corresponding author (guay@emt.inrs.ca)

Abstract

Porous electrodes based on Bismuth dendrites (Bi_{den}) were fabricated using Dynamic Hydrogen Bubbling Templates (DHBT). Direct visualization of surface-active sites with the help of advanced transmission electron microscopic (TEM) imaging reveals the presence of abundant defect structures and high-index faceting, while selective decoration of low-index facets of Bi dendrites indicate that they are the most active Bi surface sites. The fabricated electrodes show high selectivity towards CO_2 electroreduction to formate synthesis, with a 98% Faradaic Efficiency and a current density of 18.8 mA cm^{-2} ($344 \text{ } \mu\text{mol cm}^{-2} \text{ hr}^{-1}$) at -0.82 V vs RHE, which is only 600 mV more negative than the thermodynamic potential. Both the dendritic structure and CO_2 electrolysis performances are remarkably stable over long electrolysis periods (~ 15 hours). Additionally, large production rates ($1.63 \text{ mmol cm}^{-2} \text{ hr}^{-1}$ or 95 mA cm^{-2} at -0.82 V vs. RHE) without significant penalty on the formate Faradaic Efficiency ($92\% \pm 4\%$) was achieved in high-pressure flow cell, where the CO_2 flux is greatly enhanced compare to an H-cell. The work thus outlines an effective strategy for the development of dendritic materials with superior performance towards electroreduction of CO_2 .

Keywords: CO_2 electroreduction, Bi dendrites, faradaic efficiency of formate, high index facets, flow-cell.

1. Introduction

Growing emissions of carbon dioxide from human activities are driving up temperatures. This is increasing the possibility of extreme weather, melting polar ice and hastening global sea level rise. One prominent strategy to deal with rising CO₂ emissions is to convert CO₂ into value-added products by means of biochemical,[1] photochemical,[2] and electrochemical methods.[3] Electrochemical reduction of CO₂ (ERC) is one of the promising ways to remediate high levels of CO₂ emissions by converting it to useful chemicals and fuels.[3-8] The process is particularly very attractive when combined with intermittent energy sources such as solar and wind, allowing for off-the-grid energy storage that can be easily reverted back into the grid as and when needed. Among the different value-added products that can be obtained from the ERC, formate/formic acid production has generated a particular interest. The ERC to formate/formic acid is a simple two-electron process. Both chemicals are easy and safe to handle, making them useful in a variety of applications including agricultural and industrial production, livestock feed, and leather processing. It can also be used in direct formic acid fuel cell to generate electricity [9, 10] and as a mediator between electricity and microbial cultivation.[11] Formate/formic acid is selling at higher price (~2500 kWh/ton and \$1,200/ton) compared to methane (~40000 kWh/ton and \$200-\$300/ton), which needs more electrons to be produced.[12]

Several non-noble metal electrocatalysts are known to selective for the ERC to formate/formic acid: (Pb,[13-15] Sn,[16, 17] Zn,[18]). Their high selectivity ($\geq 80\%$) is accompanied by large onset potentials and high overpotentials when large current density (i.e., high production rate) is requested. Recently, Bi was considered for the ERC to formate/formic acid. Bismuth is a non-noble and earth-abundant metal with no known adverse effect on the environment. Moreover, it can be commonly obtained as a by-product in copper, lead and tin

mining industries. The faradaic efficiency for Bi varies from 81% to almost 100% in the potential range extending from -0.8 V and -1.12 V vs RHE, but the current density remains low ($< 10 \text{ mA cm}^{-2}_{\text{geo}}$). [19-23] Optimizing the structure for higher current-densities would be paramount to enhance the production rates of formate/formic acid from ERC. Zhong *et al* reported a partial current-density values of 15.2 mA cm^{-2} measured at -1.12 V vs RHE on Bi/C catalysts. [24] Yang *et al* performed similar measurements and found about 18 mA cm^{-2} at -1.1 V vs RHE on Bi nanosheets. [25] Han *et al* found 24 mA cm^{-2} at -1.06 V vs RHE on Bi nanosheets. [26] Although high current-densities were achieved in these individual cases, the observed overpotentials were still remained high. Yang *et al* have proposed that (111), (101) and (012) facets at the edges are effective for the enhanced current density. [25] However, the observed large overpotentials ($> 1 \text{ V}$) poses significant challenge. It is possible that the 2D nature of these Bi nanosheets samples constrained them from being able to achieve high-index faceting. High-index surfaces are previously shown to enhance surface structure-sensitive reactions. [27] For example, Pt high-index facets were found to increase formic acid oxidation, [22] in addition to displaying superior performances for ethanol oxidation. [28-31] Also, high-index facets of Pd were shown to maximize the electrocatalytic performances for CO_2 reduction to formate/formic acid through weakening of the CO binding affinity. [32] Elsewhere, high-index Au facets were reported to exhibit enhanced ERC activity and high selectivity to form CO. [33] Formation of high-index faceting seem to be more likely in 3D porous structures compared to 2D structures. [14, 34]

Here we demonstrate, 3D porous electrodes based on Bismuth dendrites (Bi_{den}) fabricated using Dynamic Hydrogen Bubbling Templates (DHBT). The dendritic Bi were found to be highly selective for the CO_2 electroreduction to formate with high current density of -18.8 mA cm^{-2} achievable a low-overpotential of 600 mV. High Faradaic Efficiency of 98% was achieved with a

long durability of 15 h. The defects and high-index facets were found to be most active sites where the reduction of CO₂ to formate occur. Detailed analyses of the dendrite surface-structure using atomic-resolution TEM analyses reveal that the high-index facets are more concentrated at the dendritic-tips in comparison to other regions. The in-operando active surface area measured through electrochemical impedance spectroscopy (EIS) indicates that the Bi layer is totally accessible in the CO₂ reduction process. To better estimate their performance towards more practical applications, high pressure flow-tests were also conducted. The estimated current density as large as 95 mA cm_{geo}⁻² is indicative of their high production rate of 1.63 mmol cm⁻² h⁻¹.

2. Experimental Section

2.1 Preparation of Bi dendrites

Bi dendrites (Bi_{den}) were first electrodeposited onto a Pb plate (Pb_{plate}) substrate (Nuclead, chemical grade, 1/16-inch thickness) to tune the deposition conditions and investigate their impact on the morphology of the deposit. The geometric area of the Pb plate was 0.5 cm² and the surface was electropolished to be clean and flat. The electropolishing treatment method was reported elsewhere.[14] Bi electrodeposition was carried out from a 1 mM Bi(NO₃)₃ (Sigma-Aldrich, ≥99.99% trace metals basis) and 1 M HCl (Fisher Chemical, trace metal grade) plating solution. The Bi dendrites (Bi_{den}) were galvanostatically deposited with the current densities vary from -0.1 to -0.4 A cm⁻², and deposition times vary from 1 to 40 minutes. Once the deposition conditions were optimized, the substrate was changed from Pb plate to porous Pb, Pb_{porous}. The Pb_{porous} substrate electrode was prepared by dynamic hydrogen bubbling templating (DHBT) electrodeposition at -4 A cm⁻² with the time of 40 s in a plating solution of 10 mM Pb(ClO₄)₂ + 1 M HClO₄, and the experimental details have been reported in our previous work.[14] All electrodes were rinsed with deionized water (Millipore; resistivity > 18.2 MΩ cm) and dried under a gentle

Ar stream for 30 min. A standard calomel electrode (SCE) was used as reference electrode during all these electrodeposition experiments.

2.2 Physical characterization of Bi dendrites

The surface morphology was characterized through scanning electron microscopy (SEM) (JEOL, JSM-6300F). In some cases, high-resolution field emission SEM (FE-SEM) (FEI, Magellan) was also performed. TEM observations were carried out with a FEI Titan 80-300 Cubed Scanning Transmission Electron Microscope equipped with a high-brightness field-emission electron source and ultra-fast (electron energy loss) EEL Spectrometer. Specifically, the samples were investigated under high angle annular dark field (HAADF) mode for detailed atomic-level imaging. In cases where a cross-sectional analysis of the dendritic structure needed to be carried out, an ultra-thin area was carefully lifted off using Focused Ion Beam (FIB) technique. Extreme care was taken to avoid exposure of Bi samples to air. The as-synthesized Bi samples were vacuum sealed in a glovebox immediately after preparation and before exporting to FIB-milling station, only to be loaded onto the FIB-holder again in the glovebox. X-ray diffraction (XRD) measurements were performed using a Bruker D8 Advanced with a weighted average Cu K_{α1} and Cu K_{α2} radiation at 1.5418 Å.

2.3 Electrochemical characterization of Bi dendrites

The electrochemical characterization was performed in a three-electrode cell by a Solatron 1480A multipotentiostat. A Pt gauze was chosen as the counter, and a SCE was used as electrode reference. However, all potentials in this study are quoted with respect to the Reversible Hydrogen Electrode (RHE), using the following relation $E_{\text{RHE}} = E_{\text{SCE}} + 0.241 \text{ V} + 0.059 \text{ V} \times \text{pH}$. The electrochemical active surface area (EASA) was measured in Ar-saturated (Air Liquide, 99.99%) 0.5 M KHCO₃ (Fisher Chemical, ACS Reagent) by recording the cyclic voltammograms (CVs) at

different scanning rates ranging from 80 mV s^{-1} to 1000 mV s^{-1} . The EASA of Bi_{den} was determined by calculating the double layer capacitance from $i = f(v)$ curves measured at 0.17 V (see the supplementary section). A factor of $28 \mu\text{F cm}^{-2}\text{Bi}$ was used to calculate the EASA.[19, 35] Linear sweep voltammograms (LSVs) were recorded in Ar-saturated and CO_2 -saturated 0.5 M KHCO_3 within the potential range extending from -0.32 V to -1.32 V at the scan rate of 5 mV s^{-1} .

Electrochemical impedance spectroscopy (EIS) was carried out in a three-electrode cell with the CO_2 -saturated 0.5 M KHCO_3 electrolyte. EIS measurements in the CO_2 electroreduction potential range (applied potential ranging from -0.62 to -1.22 V by steps of 0.5 V) were obtained between 0.01 Hz and 200 kHz using a FRA Analyser (Solartron 1255B). In all cases, the current was allowed to stabilize for 30 minutes (see below) before starting the EIS measurements. Fitting to the equivalent circuit was carried out by using Zview.

The products were analyzed after 30 min electrolysis of CO_2 at the potential ranging from -0.62 V to -1.22 V . Formate concentration was measured by ion chromatography (IC) (ICS-1500, Dionex, USA) using an IonPac AS9-HC column separation column with a $9 \text{ mM Na}_2\text{CO}_3$ mobile phase at a flow rate of 1 mL/min . All samples were diluted 10 times before measurement. Gas products were analyzed by gas chromatography (GC) (Agilent Micro 490) at two channels with the thermal conductivity detector. Only formate and H_2 were detected and the total Faradaic efficiency (FE) was $100 \pm 5\%$.

2.4 Flow-cell

A flow-cell was designed to test the catalyst's CO_2 reduction capability under higher CO_2 flux. A schematic representation of the flow-cell is shown in Figure 7a. The core of the electrolysis cell where the working electrode, the Nafion 117 separating membrane and the anode is shown in the enlarged view of the cell shown in Figure 7b. This flow-cell is equipped with a Saturated

Calomel Electrode (SCE) reference and a Pt gauze counter electrode. Both the working and counter electrodes have a disk shape with a geometric surface of 1 cm². In this setup, the catholyte and anolyte flow rate (Masterflex L/S Easy-Load[®] II Model 77200-50 pump head and 06434-17 pump tube) and pressure can be controlled independently. A Bi_{den}/Pb_{porous} electrode was used as cathode. The electrolyte was a CO₂ super-saturated 0.5 M KHCO₃ solution that was prepared by using a soda machine (Sodastream, CO₂ purity 99.999%). The catholyte was circulated at a flow rate of 104 ± 1 mL min⁻¹ and the catholyte pressure was 5 psig. The anolyte was 0.5 M KHCO₃. It was circulated at a flow rate of 2.3 ± 1 mL min⁻¹ and the anolyte back pressure was 6 psig.

3. Results and Discussion

3.1 Optimization and physiochemical characterization of the deposition conditions of Bi dendrites

Pb was chosen as a substrate because (i) it is less active than Bi for the ERC, (ii) not a good catalysis for the hydrogen evolution reaction, and (iii) can be prepared in a porous form that provides an extended surface area for the subsequent deposition of Bi.

The Bi deposition conditions were first optimized on a (dense and flat) Pb plate, Pb_{plate}. Different deposition current densities (from -0.1 to -0.4 A cm⁻²) and deposition times (from 1 to 40 minutes) were investigated (Figure S1). At these deposition current densities, the deposition potentials varied from -1.1 to -1.4 V vs RHE, and simultaneous Bi deposition and hydrogen evolution occur. Electrodeposition under these conditions is referred to as “Dynamic Hydrogen Bubble Templating” (DHBT).[36-39] The Bi electrochemically active surface area, Bi EASA, was determined through cyclic voltammetry experiments in Ar-saturated 0.5 M KHCO₃. The capacitive current was measured as a function of the sweep rate in a potential region where only double-layer charge/discharge processes occur (see Figure S2a). As seen in Figure S2b, the Bi EASA increases

linearly with deposition current densities. Likewise, the Bi EASA increases steadily, although not linearly, with deposition times (see Figure S2c).

SEM micrographs of Bi deposited at -0.4 A cm^{-2} on Pb_{plate} for 40 minutes (and giving the largest Bi EASA) are presented in Figure 1. The Bi deposit is very porous. It has a honeycomb-like primary structure with surface pores *ca.* $150 \text{ }\mu\text{m}$ in diameter (Figure 1a). This structure is characteristic of films prepared by electrodeposition under vigorous hydrogen evolution (DHBT deposition conditions). At higher magnification (Figure 1c and 1d), the Bi deposit's secondary structure is clearly observed; it is composed of dendrites consisting of stems to which branches are attached. The measured length of the stems is *ca* $1 \text{ }\mu\text{m}$. As shall be discussed later in Figure 2, detailed TEM analyses of these individual branches suggest their dimensions to be about 15 nm in diameter and 70 nm in length. All branches and stems terminate with sharper tips apparent as spherical contours in the SEM images (radius = $5.4 \pm 1.0 \text{ nm}$, see Figure S3, in reasonably good agreement with the 7.5 nm radius determined later on by HR-TEM analysis). In the subsequent discussions, we will refer to bismuth deposited in these conditions as dendritic Bi, Bi_{den} .

After further optimization of these synthetic conditions, the Bi deposition conditions were fixed at -0.4 A cm^{-2} for 40 minutes but the substrate was changed from a flat Pb plate to a highly porous Pb substrate ($\text{Pb}_{\text{porous}}$). The later substrate was prepared based on previously-determined experimental conditions ($10 \text{ mM Pb}(\text{ClO}_4)_2 + 1 \text{ M HClO}_4$, 4 A cm^{-2} deposition current density and a 40-second deposition time).[14] Deposition in these conditions (DHBT deposition conditions) yields a very porous Pb substrate (Figure S4) whose morphology is similar (although not identical) to that of the dendritic Bi deposit. The dendritic nature of Pb substrate is clearly evidenced in Figure 1e and 1f, which show very distinctive morphology of the underlying porous Pb electrode and dendritic Bi. It is clear that regions of the underlying porous Pb substrate are not covered with

Bi dendrites. However, the morphology of those regions which are covered with Bi dendrites are identical to those observed when Bi deposition is performed on a flat (Pb plate) substrate (see Figure 1g) indicating that the formation of the Bi dendritic structure is not affected by the increased porosity of the underlying substrate. The cross-sectional micrograph of this electrode (Figure 1h) reveals that the Bi dendrites formed are not constrained to the surface regions but rather penetrate deep into porous regions of the underlying Pb substrate. This will prove to be important later on.

Figure 2a illustrates atomic-resolution image of a typical Bi dendrite, $\sim 15\text{ nm}$ in diameter and $\sim 70\text{ nm}$ in length, as evidenced by the low-magnification TEM image shown in Figures 2a-b. The dendritic orientation is determined by comparison to series of reported Bi phases and lattice distances (ICSD codes #64703, #51674 and #189806, as such). As shown in Figures 2c-d, a satisfactory match is achieved for the Bi rhombohedral structure (Space group: R-3m) oriented along [010] growth direction and viewed along plane normal to (100). Similarities in the structure are further obvious from a direct visual comparison of the two images. Figure 2e illustrates the dendrite structure with specific focus onto the surface-structure. The atomic-structure revealed and the lattice-distances measured therein show that the rhombohedral structure of Bi in the core is preserved even at the top-most surface layers. No obvious displacements in the surface atoms suggesting binding with oxygen or other contaminants could be determined. These observations ascertain that the Bi needles considered in our work is mostly pristine, expected since extreme care was taken to avoid any sample exposure to oxidation.

As can be seen in Figure 2e, the terminated dendrite surface is not entirely smooth (yellow arrows), but has surface irregularities in the form of ‘surface-steps’ (green arrows). Previously, such surface-irregularities have shown to play a key role in enhancing electrochemical reactivities of Pd for formate oxidation,[40] which is the reverse reaction to the one considered in the present

work. In a first approximation, the surface occupied by the tips of the dendrite is given by D / L , where D is the dendrite diameter and L the length of the straight sections. Based on the data of Figure 2b, $D / L \sim 20\%$. The concentration of these surface steps and high-index facets is higher at the tips ($\sim 20\%$ of the dendrite surface) than on the straight sections ($\sim 80\%$ of the dendrite surface). It will be shown experimentally later on that these surface irregularities are playing a crucial role in the high activity of Bi dendrites for the ERC.

XRD patterns of dendritic Bi deposits prepared in different deposition conditions are outlined in Figures S5a-b. For comparison, the position of the diffraction peaks of Bi, Bi_2O_3 and Pb are also shown. As evident from these XRD traces, there is no trace of bismuth oxide. Indeed, Bi dendrites are made of metallic (rhombohedral) Bi, although the relative intensities of the diffraction peaks differ from polycrystalline Bi. For example, the peak intensity of high-index planes such as (102) is exacerbated, suggesting a preferential texturing of Bi_{den} at the surface of the substrate.

To verify this observation, the texture coefficient ($TC_{(hkl)}$) of the thickest film was calculated by the inverse pole intensity technique using the following equation:[41]

$$TC_{(hkl)} = \frac{I_{(hkl)} / I_{R(hkl)}}{\frac{1}{n} \sum_i^n (I_{(hkl)} / I_{R(hkl)})}$$

where $I_{(hkl)}$ is the reflected intensity from (hkl) crystallographic planes in the textured specimen, $I_{R(hkl)}$ is the reflected intensity from (hkl) crystallographic planes from the random specimen, and n is the total number of reflections measured. $TC_{(hkl)}$ is proportional to the number of grains oriented with the (hkl) plane parallel to the surface. $TC_{(hkl)} > 1$ (< 1) denotes samples that have more (less) crystallites oriented in the (hkl) direction than randomly oriented polycrystalline Bi. As seen in Figure S5a-b, $TC_{(102)} > 1$ and $TC_{(122)} < 1$, indicating the family of planes in (102)

direction, are over represented in the Bi dendritic deposit (compared to polycrystalline Bi). As seen in Figure S5c, only the (102) and (122) peaks have TC values that deviate by more than 20% from unity. As we are going to see later on, Bi dendrites are growing along the [010] zone axis. The angle between the (102) planes and the [010] growth axis is 90° and accordingly, a significant fraction of Bi dendrites have their growth axis oriented parallel to the surface of the substrate. Consistently, $TC_{(122)}$ is less than 1 since the (122) planes are perpendicular to the (102) planes. A schematic representation of the growth of Bi dendrites is depicted in Figure S5d, alongside a SEM micrograph of the early stage of Bi deposition that emphasizes regions where the [001] growth axis of dendritic Bi is parallel to the flat Pb substrate.

3.2 Catalytic activity of Bi dendrites and the Pb substrate effect

An evaluation of the electrocatalytic activity of Bi_{den} was first achieved through potentiodynamic measurements (5 mV s^{-1}) in CO_2 -saturated 0.5 M KHCO_3 electrolyte at $\text{pH} = 7.33$. In Figure 3a and S6, linear sweep voltammograms (LSVs) show that the onset potentials for ERC at both Bi_{den} electrodes are identical (*ca.* -0.54 V) and independent of the nature of the underlying Pb substrates. On the contrary, the current densities, j , at $\text{Bi}_{\text{den}}/\text{Pb}_{\text{porous}}$ are always larger than at $\text{Bi}_{\text{den}}/\text{Pb}_{\text{plate}}$. It is noteworthy that the onset potentials of Bi_{den} electrodes are smaller, and the total current density are larger, compared to bare lead substrates, emphasizing the critical role dendritic Bi plays in achieving high electrocatalytic activity. For comparison, the ERC onset potential on porous Pb is -0.65 V , which is 110 mV more negative than for Bi_{den} , while the current density of $\text{Pb}_{\text{porous}}$ is at least a factor 10 lower than for electrodes covered with dendritic Bi.

To further explore the catalytic performance of dendritic Bi, the products formed at different potential values during CO_2 reduction were analyzed after 30 minutes of electrolysis. In all cases, only formate (Figure 3b) and H_2 (Figure 3c) were detected, and the total faradaic

efficiency (FE) reached $100 \pm 5\%$. As seen in Figure 3b, there was no difference between the FE_{formate} vs. potential curves of dendritic Bi deposited on the two different substrates (Pb_{plate} and Pb_{porous}). In both cases, the maximum FE_{formate} value is 98% and is attained at -0.82 V vs RHE. This is 200 mV more positive than the potential at which the largest value of FE_{formate} is attained on the Pb_{porous} substrate alone. In the case of the Pb_{plate} substrate, FE_{formate} values larger than 80% were never reached even at the more negative potential studied here.

The partial current densities of formate, j_{formate} , which are exclusively associated with formate production, are shown in Figure 3d. The j_{formate} values of dendritic Bi deposited on both Pb substrates increase steadily in the low overpotential regime (from -0.6 to -0.9V) to reach a plateau at more negative potential ($\leq -0.9V$). The j_{formate} plateau value of $Bi_{\text{den}}/Pb_{\text{porous}}$ is $\sim 27 \text{ mA cm}^{-2}$, almost 1.6-fold higher than on $Bi_{\text{den}}/Pb_{\text{plate}}$ ($\sim 17 \text{ mA cm}^{-2}$). As shown in Figure 1h, Bi dendrites are deposited in regions of the porous Pb_{den} substrate that are inaccessible on a dense Pb_{plate} substrate. Accordingly, even if the deposition conditions used for the preparation of dendritic Bi are rigorously identical, there are more Bi dendrites accessible to the electrolyte on $Bi_{\text{den}}/Pb_{\text{porous}}$ than on $Bi_{\text{den}}/Pb_{\text{plate}}$. This is nicely confirmed by the Bi EASA of $Bi_{\text{den}}/Pb_{\text{porous}}$ (231 cm^2), which is *ca.* 1.5-fold larger than $Bi_{\text{den}}/Pb_{\text{plate}}$ (156 cm^2) (see Figure S9). Indeed, the LSV and the j_{formate} curves of $Bi_{\text{den}}/Pb_{\text{plate}}$ and $Bi_{\text{den}}/Pb_{\text{porous}}$ are almost superimposed on each other when normalized to the Bi EASA (see Figure S10). The Bi EASA is determined through CV measurements in a potential region involving double-layer charge/discharge processes, which are not limited by diffusion. On the contrary, the j_{formate} plateau value is measured in a potential region where CO_2 reduction (faradaic reaction) is occurring. This faradaic reaction is dependent on the diffusion of CO_2 to the reaction site. The fact that j_{formate} scales exactly like the Bi EASA indicates that all available active Bi active sites are accessible and participating in the faradaic reaction. Therefore,

even if the deposition conditions are optimized to promote the formation of a porous dendritic Bi deposit, it is still possible to further increase the areal density of available active sites by using a porous ($\text{Pb}_{\text{porous}}$) instead of a flat substrate (Pb_{plate}).

It was shown previously that the current density difference between $\text{Bi}_{\text{den}}/\text{Pb}_{\text{porous}}$ and $\text{Bi}_{\text{den}}/\text{Pb}_{\text{plate}}$ can be rationalized based on the different (3D) structure of both lead substrates. On the contrary, both electrodes exhibit the same ERC onset potentials. This makes sense since the onset potential of a reaction (reduction/oxidation) is the least (negative/positive) potential that should be applied for the reaction to occur (at very low rate and thus very low current density). In that sense, it is not expected that the onset potential will be affected by the EASA. On the contrary, the onset potential is dependent on the nature of the materials but, more importantly for the present study, on its microstructure. So, on Bi flakes, which are formed by electrodeposition at much lower deposition overpotential (50 mV) and thus much lower current density, the onset potential for the ERC is -0.7 V vs. RHE,[14] which is 160 mV more negative than on Bi dendrites.

In order to clearly correlate the ERC property to the 3D structure of dendritic Bi, a series of EIS measurements was performed. The impedance spectra of Figure S11 shows the classic features of a solution resistance in series with a parallel combination of a constant-phase element representing the double layer and a charge-transfer resistance. The effective double-layer capacitance C_{eff} was obtained from the CPE parameters and the parallel combination of the two resistances using the Brug formula.[42]

A Tafel analysis of the best performing electrode ($\text{Bi}_{\text{den}}/\text{Pb}_{\text{porous}}$) is given in Figure 4. The EIS measurements were carried out at various electrode potentials ranging from -0.62 to -1.07 V vs. RHE. Before each EIS measurement, a potentiostatic current was recorded for 30 min and it reached to a steady state value. These current (j) data points were used to obtain the value of Tafel

slope (as shown in Figure 4a). The Tafel slope is 156 mV dec^{-1} in the kinetically limited region (potential more positive than -0.75 V). In the region between -0.75 and -0.90 , j is almost constant, indicating the reaction reaches its mass transport limitations. At potential more negative than -0.9 V , j increases again, most probably because the hydrogen evolution reaction becomes predominant. This is consistent with the FE_{H_2} starting to increase (Figure 3c) and the EIS data becoming noisier (Figure S11) at potentials more negative than -0.87 V . As the applied potential is more negative, R_{ct} initially decreases (see Table S1), with an exponential (Tafel) potential dependence as expected since $R_{\text{ct}} \approx R_{\text{p}}$. The slope of $\log(1/R_{\text{ct}})$ vs potential curves is 147 mV dec^{-1} (Figure 4b), very similar to the Tafel slope determined from j values. C_{eff} does not vary with potential (Figure 4c), even when the current is limited by CO_2 mass-transport or increased due to the HER. The mean C_{eff} value is $6.1 \pm 0.4 \text{ mF cm}^2_{\text{geo}}$, a factor *ca* 215 larger than the specific capacitance of Bi ($28 \mu\text{F cm}^2$). This value is close to the roughness factor of 231 determined from CVs measurements in a potential region where no faradic reaction is occurring, indicating that the same electrode surface is accessed in both cases. For comparison, C_{eff} of $\text{Bi}_{\text{den}}/\text{Pb}_{\text{plate}}$ is also invariant with the electrode potential (see Figure S12), with a mean value of $4.1 \pm 0.2 \text{ mF cm}^2_{\text{geo}}$, which is a factor of *ca* 1.5 lower than $\text{Bi}_{\text{den}}/\text{Pb}_{\text{porous}}$. The Bi EASA and C_{eff} values are consistently supporting the view that part of the electrode that would not be easily reached by the electrolyte and dissolved CO_2 are readily accessible upon depositing Bi_{den} on a porous substrate.

3.3 Electrode stability

Aside from onset potential, overpotential, current density, and current efficiency (which, taken together, have an impact on the energy efficiency of the process), stability is another critical issue for electrodes in the development of an ERC process. Figures 5a and 5b demonstrate that both the total current density (-18.8 mA cm^{-2}) and faradaic efficiency ($\geq 95\%$) remained constant

during a long-term (15 hours) electrolysis test performed at -0.82 V. This indicates that stable operation can be achieved in terms of both current density and selectivity, and that contamination of the electrode surface during electrolysis is not an issue. In the literature, contamination/modification of the electrode surface through electrodeposition of foreign elements contained in the aqueous electrolyte, or even adsorption of carbonaceous compounds, have often been invoked to explain performance degradation (electrode potential, current density and/or faradic efficiency) over time.[43, 44] This is not the case in the present study, where the electrode's dendritic structure and large Bi EASA may help mitigate this poisoning effect (if any). This might occur because the number of catalytic sites that are poisoned (and thus not available for the ERC) is small compared to the initial number; alternately, as it will be demonstrated by the intentional deposition of Pb on Bi dendrites, electrodeposition/adsorption of contaminants may be occurring at sites that are less active for the ERC. This is certainly contributing to maintaining a stable electrocatalytic activity for the ERC over a long period. Finally, it is worth noting that the morphology of Bi dendrites remains unchanged even after 15 hours of electrolysis (Figures 5c and 5d), indicating that the electrode structure is not collapsing during sustained operation, which again demonstrates the stability of the electrode.

3.4 Identification of Bi active sites for high selectivity and long durability

To identify the Bi catalytic sites, we undertook to mask selectively certain a fraction of them with a less active material (Pb) for the ERC to formate. To achieve this, Bi_{den} was first electrodeposited. After recording the Bi EASA and the ERC current at -0.82 V vs RHE in CO₂-saturated 0.5 M KHCO₃ electrolyte, the Bi_{den} sample was rinsed and transferred to a 1 mM Pb(ClO₄)₂ and 0.1 M HClO₄ plating solution. Then, plating of Pb was carried out by applying a series of potentiostatic pulses, with $E_{on} = -0.48$ V vs SCE with $T_{on} = 1$ s, and $E_{off} = OCP$ with T_{off}

= 10s. This potentiostatic pulse sequence was chosen to prevent Pb from being deposited under mass-transport limited conditions (see Figure S13). Pb deposition was performed by changing only the number of pulses (from 120 to 760 cycles) to vary the amount of deposited Pb. The EASA of Bi_{den} covered with various amounts of Pb was then measured and the activity for the ERC was assessed again. It is known from the Pb underpotential deposition (UPD) literature that anions in the plating solution can be strongly adsorbed on defects present at an electrode surface, thereby preventing Pb deposition at these high energy sites and favoring it at low index facets and defect-free sites.[45-47]

As seen in Figure 6a, the percent of Bi EASA loss varies linearly with the number Pb deposition cycle. This indicates that every addition of Pb is as effective as the previous ones in masking a constant fraction of the Bi dendritic surface. Almost 75% of the Bi EASA is lost after 800 cycles of Pb deposition. Likewise, the loss of ERC activity (Figure 6b) varies linearly with the number of pulses. However, the most interesting piece of information is depicted in Figure 6, which shows the variation of percent loss of ERC with respect to the percent loss of Bi EASA. Three regions were identified. The blue line depicts the behavior expected if Pb was deposited on Bi sites that are equally active for the ERC (a loss of Bi EASA translate into an equivalent loss of ERC). The section of the graph located above and below that blue line indicates regions where the Bi active sites are not all equivalent, and data points in the region below (above) the blue line indicate that Pb is deposited on Bi sites that are not (that are) the most active for the ERC. As seen in Figure 6c, there is effectively a linear relationship between the EASA loss and the ERC loss (the slope is 0.36), but all data points are below the blue line. This means that not all Bi surface sites are equivalent for the ERC and that Pb atoms deposit preferentially on the less active Bi surface sites.

Geometrical considerations based on the HRTEM micrograph of Figure 2 help us to unravel the structure of the most active Bi sites. As seen in Figure 2, the surface concentration of defects is larger at the tip of the dendrite than on their walls. Since the deposition of Pb was performed in UPD conditions, the defect-free Bi sites, which account for more than 80% of the dendrite surface, are supposed to be covered by Pb rather than the active tip sites. Accordingly, the covered defect-free Bi sites would be responsible for a significant decrease of the Bi EASA without causing a proportional change of the ERC activity. The most active Bi sites would be those that account for the smallest fraction of the dendrite surface area that is not covered by Pb in the UPD process. This assertion is consistent with the most recent DFT calculations made by Koh *et al.* showing that high-index (012), (110) and (104) facets stabilize HCOO* more than the compact (003) plane.[22]

3.5 Continuous flow-cell test of the Bi_{den}/Pb_{porous} electrode

To increase the production rate of formate, a flow-cell was designed to test the CO₂ reduction capability of Bi_{den}/Pb_{porous} electrodes in conditions where large CO₂ flux can be achieved. A schematic representation of the flow-cell is shown in Figure 7. As detailed in the experimental section, the electrolyte was super saturated with CO₂. The average current density was 95 mA cm⁻² at -0.82 V vs. RHE and was constant over the long-term electrolysis test (5 h) we performed (see Figure 7c). Also important, the $FE_{formate}$ was 92%±4%, very close to the value observed in the H-cell. Compared with the 344 μmol cm⁻² hr⁻¹ formate production rate in the H-cell, the production rate in the flow-cell test was 1.63 mmol cm⁻² hr⁻¹, which is around 5-fold larger. This increased current density compared to the H-cell results from overcoming the CO₂ mass transport limitation through increased flow rate and increased amount of CO₂ (oversaturation) in the electrolyte. A detailed comparison of the ERC performances of different Bi-based electrodes is shown in Table

S2. It emphasizes that Bi_{den}/Pb_{porous} electrodes, thanks to their atomic surface structure with defects and high-index facets, can sustain large current densities and achieve large formate production rate if they are operated in a regime that is not limited by the diffusion of CO₂.

4. Conclusion

In summary, dendritic Bi electrode with a large amount of defects and high-index facets was synthesized on a porous Pb substrate. The identification of the most active Bi sites was performed through a detailed atomic scale analysis of the surface of the dendrite and masking of the low-index inactive sites. It was shown that defects and high-index facets of Bi dendrites are the most active sites where the reduction of CO₂ to formate occurred. Dendritic Bi is highly selective for the CO₂ electroreduction to formate with a 98% Faradaic Efficiency and a current density of 18.8 mA cm⁻² (344 μmol cm⁻² hr⁻¹) at -0.82 V vs RHE, which is only 600 mV more negative than the thermodynamic potential. Both the dendritic structure and CO₂ electrolysis performances are remarkably stable over the longest electrolysis (15 hours) we have conducted. Additionally, much larger production rate (1.63 mmol cm⁻² hr⁻¹ or 95 mA cm⁻² at -0.82 V vs. RHE) without any major penalty on the formate Faradaic Efficiency (92%±4%) was achieved with the same electrode operated in conditions where the CO₂ flux is not limiting its performances (high-pressure flow-cell measurements). This work presents a simple method to design and fabricate materials in dendritic form with excellent performances for the ERC. It also provides atomic scale insights into the nature of the active sites at the surface of dendrites. Finally, it illustrates that dendritic electrode materials are able to withstand very large current density and thus achieve very large production rate if the CO₂ supply to the electrode is not limiting.

Acknowledgement

This work was supported by the Natural Sciences and Engineering Research Council of Canada (NSERC) and the Canada Research Chair program. This research was conducted as part of the Engineered Nickel Catalysts for Electrochemical Clean Energy project administered from Queen's University and supported by Grant No. RGPNM 477963-2015 under the Natural Sciences and Engineering Research Council of Canada (NSERC) Discovery Frontiers Program. M. F. acknowledges "Fonds Recherche du Québec - Nature et Technologies" (FRQ-NT) for a Graduate Research Fellowship supporting this work.

References

- [1] A.M. Appel, J.E. Bercaw, A.B. Bocarsly, H. Dobbek, D.L. DuBois, M. Dupuis, J.G. Ferry, E. Fujita, R. Hille, P.J. Kenis, C.A. Kerfeld, R.H. Morris, C.H. Peden, A.R. Portis, S.W. Ragsdale, T.B. Rauchfuss, J.N. Reek, L.C. Seefeldt, R.K. Thauer, G.L. Waldrop, Frontiers, Opportunities, and Challenges in Biochemical and Chemical Catalysis of CO₂ Fixation, *Chem. Rev.*, 113 (2013) 6621-6658.
- [2] J.L. White, M.F. Baruch, J.E. Pander Iii, Y. Hu, I.C. Fortmeyer, J.E. Park, T. Zhang, K. Liao, J. Gu, Y. Yan, T.W. Shaw, E. Abelev, A.B. Bocarsly, Light-Driven Heterogeneous Reduction of Carbon Dioxide: Photocatalysts and Photoelectrodes, *Chem. Rev.*, 115 (2015) 12888-12935.
- [3] C. Costentin, M. Robert, J.M. Saveant, Catalysis of the Electrochemical Reduction of Carbon Dioxide, *Chem. Soc. Rev.*, 42 (2013) 2423-2436.
- [4] J. Gong, L. Zhang, Z.J. Zhao, Nanostructured Materials for Heterogeneous Electrocatalytic CO₂ Reduction and Related Reaction Mechanisms, *Angew. Chem. Int. Ed. Engl.*, 129 (2017) 11482-11511.
- [5] J. Qiao, Y. Liu, F. Hong, J. Zhang, A Review of Catalysts for the Electroreduction of Carbon Dioxide to Produce Low-carbon Fuels, *Chem. Soc. Rev.*, 43 (2014) 631-675.
- [6] E.E. Benson, C.P. Kubiak, A.J. Sathrum, J.M. Smieja, Electrocatalytic and Homogeneous Approaches to Conversion of CO₂ to Liquid Fuels, *Chem. Soc. Rev.*, 38 (2009) 89-99.
- [7] D. T. Whipple, P. J. A. Kenis, Prospects of CO₂ Utilization via Direct Heterogeneous Electrochemical Reduction, *J. Phys. Chem. Lett.*, 1 (2010) 3451-3458.
- [8] Y. Zheng, W. Zhang, Y. Li, J. Chen, B. Yu, J. Wang, L. Zhang, J. Zhang, Energy Related CO₂ Conversion and Utilization: Advanced Materials/Nanomaterials, Reaction Mechanisms and Technologies, *Nano Energy*, 40 (2017) 512-539.

- [9] M. Aresta, A. Dibenedetto, A. Angelini, Catalysis for the Valorization of Exhaust Carbon: from CO₂ to Chemicals, Materials, and Fuels. Technological Use of CO₂, Chem. Rev., 114 (2014) 1709-1942.
- [10] X. Yu, P.G. Pickup, Recent advances in direct formic acid fuel cells (DFAFC), J. Power Sources 182 (2008) 124-132.
- [11] O. Yishai, S.N. Lindner, J. Gonzalez de la Cruz, H. Tenenboim, A. Bar-Even, The Formate Bio-economy, Curr. Opin. Chem. Biol., 35 (2016) 1-9.
- [12] J. Durst, A. Rudnev, A. Dutta, Y. Fu, J. Herranz, V. Kaliginedi, A. Kuzume, A.A. Permyakova, Y. Paratcha, P. Broekmann, T.J. Schmidt, Electrochemical CO₂ Reduction - A Critical View on Fundamentals, Materials and Applications, Chimia, 69 (2015) 769-776.
- [13] C.H. Lee, M.W. Kanan, Controlling H⁺ vs CO₂ Reduction Selectivity on Pb Electrodes, ACS Catal., 5 (2015) 465-469.
- [14] M. Fan, S. Garbarino, G.A. Botton, A.C. Tavares, D. Guay, Selective Electroreduction of CO₂ to Formate on 3D [100] Pb Dendrites with Nanometer-sized Needle-like Tips, J. Mater. Chem. A, 5 (2017) 20747-20756.
- [15] B. Eneau-Innocent, D. Pasquier, F. Ropital, J.M. Léger, K.B. Kokoh, Electroreduction of carbon dioxide at a lead electrode in propylene carbonate: A spectroscopic study, Appl. Catal. B-Environ., 98 (2010) 65-71.
- [16] S. Zhang, P. Kang, T.J. Meyer, Nanostructured Tin Catalysts for Selective Electrochemical Reduction of Carbon Dioxide to Formate, J. Am. Chem. Soc., 136 (2014) 1734-1737.
- [17] J.E. Pander, M.F. Baruch, A.B. Bocarsly, Probing the Mechanism of Aqueous CO₂ Reduction on Post-Transition-Metal Electrodes using ATR-IR Spectroelectrochemistry, ACS Catal., 6 (2016) 7824-7833.

- [18] T. Zhang, H. Zhong, Y. Qiu, X. Li, H. Zhang, Zn Electrode with a Layer of Nanoparticles for Selective Electroreduction of CO₂ to Formate in Aqueous Solutions, *J. Mater. Chem. A*, 4 (2016) 16670-16676.
- [19] E. Bertin, S. Garbarino, C. Roy, S. Kazemi, D. Guay, Selective Electroreduction of CO₂ to Formate on Bi and Oxide-Derived Bi Films, *J. CO₂ UTIL.*, 19 (2017) 276-283.
- [20] S. Kim, W.J. Dong, S. Gim, W. Sohn, J.Y. Park, C.J. Yoo, H.W. Jang, J.-L. Lee, Shape-Controlled Bismuth Nanoflakes as Highly Selective Catalysts for Electrochemical Carbon Dioxide Reduction to Formate, *Nano Energy*, 39 (2017) 44-52.
- [21] Y. Qiu, J. Du, W. Dong, C. Dai, C. Tao, Selective Conversion of CO₂ to Formate on a Size Tunable Nano-Bi Electrocatalyst, *J. CO₂ UTIL.*, 20 (2017) 328-335.
- [22] J.H. Koh, D.H. Won, T. Eom, N.-K. Kim, K.D. Jung, H. Kim, Y.J. Hwang, B.K. Min, Facile CO₂ Electro-Reduction to Formate via Oxygen Bidentate Intermediate Stabilized by High-Index Planes of Bi Dendrite Catalyst, *ACS Catal.*, 7 (2017) 5071-5077.
- [23] X. Zhang, T. Lei, Y. Liu, J. Qiao, Enhancing CO₂ Electrolysis to Formate on Facilely Synthesized Bi Catalysts at Low Overpotential, *Appl. Catal. B-Environ.*, 218 (2017) 46-50.
- [24] H. Zhong, Y. Qiu, T. Zhang, X. Li, H. Zhang, X. Chen, Bismuth Nanodendrites as a High Performance Electrocatalyst for Selective Conversion of CO₂ to Formate, *J. Mater. Chem. A*, 4 (2016) 13746-13753.
- [25] H. Yang, N. Han, J. Deng, J. Wu, Y. Wang, Y. Hu, P. Ding, Y. Li, Y. Li, J. Lu, Selective CO₂ Reduction on 2D Mesoporous Bi Nanosheets, *Adv. Energy Mater.*, 8 (2018) 1801536.
- [26] N. Han, Y. Wang, H. Yang, J. Deng, J. Wu, Y. Li, Y. Li, Ultrathin Bismuth Nanosheets from In Situ Topotactic Transformation for Selective Electrocatalytic CO₂ Reduction to Formate, *Nat. Commun.*, 9 (2018) 1320.

- [27] J. Solla-Gullón, F.J. Vidal-Iglesias, J.M. Feliu, Shape Dependent Electrocatalysis, *Annu. Rep. Prog. Chem., Sect. C*, 107 (2011) 263.
- [28] N. Tian, Z.-Y. Zhou, S.-G. Sun, Y. Ding, Z.L. Wang, Synthesis of Tetrahedral Platinum Nanocrystals with High-Index Facets and High Electro-Oxidation Activity, *Science*, 316 (2007) 732-735.
- [29] X. Huang, Z. Zhao, J. Fan, Y. Tan, N. Zheng, Amine-Assisted Synthesis of Concave Polyhedral Platinum Nanocrystals Having {411} High-index Facets, *J. Am. Chem. Soc.*, 133 (2011) 4718-4721.
- [30] Z.Y. Zhou, Z.Z. Huang, D.J. Chen, Q. Wang, N. Tian, S.G. Sun, High-index Faceted Platinum Nanocrystals Supported on Carbon Black as Highly Efficient Catalysts for Ethanol Electrooxidation, *Angew. Chem. Int. Ed. Engl.*, 49 (2010) 411-414.
- [31] J. Zhang, L. Zhang, S. Xie, Q. Kuang, X. Han, Z. Xie, L. Zheng, Synthesis of Concave Palladium Nanocubes with High-index Surfaces and High Electrocatalytic Activities, *Chem. Eur. J*, 17 (2011) 9915-9919.
- [32] A. Klinkova, P. De Luna, C.-T. Dinh, O. Voznyy, E.M. Larin, E. Kumacheva, E.H. Sargent, Rational Design of Efficient Palladium Catalysts for Electroreduction of Carbon Dioxide to Formate, *ACS Catal.*, 6 (2016) 8115-8120.
- [33] H.-E. Lee, K.D. Yang, S.M. Yoon, H.-Y. Ahn, Y.Y. Lee, H. Chang, D.H. Jeong, Y.-S. Lee, Y.-S. Kim, K.T. Nam, Concave Rhombic Dodecahedral Au Nanocatalyst with Multiple High-Index Facets for CO₂ Reduction, *ACS Nano*, 9 (2015) 8384–8393.
- [34] A. Kumar, J.M. Gonçalves, J.S.G. Selva, K. Araki, M. Bertotti, Correlating Selective Electrocatalysis of Dopamine and Ascorbic Acid Electrooxidation at Nanoporous Gold Surfaces with Structural-Defects, *J. Electrochem. Soc.*, 166 (2019) H704-H711.

- [35] V. Ivaništšev, R.R. Nazmutdinov, E. Lust, Density Functional Theory Study of the Water Adsorption at Bi(111) Electrode Surface, *Surf. Sci.*, 604 (2010) 1919-1927.
- [36] H.-C. Shin, J. Dong, M. Liu, Nanoporous Structure Prepared by an Electrochemical Deposition Process, *Adv. Mater.*, 15 (2003) 1610-1614.
- [37] B.J. Plowman, L.A. Jones, S.K. Bhargava, Building with Bubbles: the Formation of High Surface Area Honeycomb-like Films via Hydrogen Bubble Templated Electrodeposition, *Chem. Commun.*, 51 (2015) 4331-4346.
- [38] Y. Li, W.-Z. Jia, Y.-Y. Song, X.-H. Xia, Superhydrophobicity of 3D Porous Copper Films Prepared Using the Hydrogen Bubble Dynamic Template, *Chem. Mater.*, 19 (2007) 5758-5764.
- [39] L.D. Rafailović, C. Gammer, C. Rentenberger, T. Trišović, C. Kleber, H. Peter Karnthaler, Enhanced Oxygen Evolution and Reduction Reactions of Porous Ternary NiCoFe Foam Electrodes Prepared by Dynamic Hydrogen Template Deposition, *Nano Energy*, 2 (2013) 523-529.
- [40] S. Patra, B. Viswanath, K. Barai, N. Ravishankar, N. Munichandraiah, High-surface Step Density on Dendritic Pd Leads to Exceptional Catalytic Activity for Formic Acid Oxidation, *ACS Appl. Mater. Interfaces.*, 2 (2010) 2965-2969.
- [41] E. Moran, C. Cattaneo, H. Mishima, B.A. López de Mishima, S.P. Silveti, J.L. Rodriguez, E. Pastor, Ammonia Oxidation on Electrodeposited Pt–Ir Alloys, *J. Solid State Electr.*, 12 (2007) 583-589.
- [42] G.J. Brug, A.L.G. van den Eeden, M. Sluyters-Rehbach, J.H. Sluyters, The Analysis of Electrode Impedances Complicated by the Presence of a Constant Phase Element, *J. Electroanal. Chem.*, 176 (1984) 275-295.
- [43] Y. Hori, H. Konishi, T. Futamura, A. Murata, O. Koga, H. Sakurai, K. Oguma, “Deactivation

of Copper Electrode” in Electrochemical Reduction of CO₂, *Electrochim. Acta*, 50 (2005) 5354-5369.

[44] P. Friebe, P. Bogdanoff, N. Alonso-Vante, H. Tributsch, A Real-Time Mass Spectroscopy Study of the (Electro)chemical Factors Affecting CO₂ Reduction at Copper, *J. Catal.*, 168 (1997) 374–385.

[45] V. D. Jović, B. M. Jović, A. R. Despić, The Influence of Solution Composition on Lead, Cadmium and Thallium Underpotential Deposition on (111) Oriented Silver Single Crystal Surfaces, *J. Electroanal. Chem.*, 288 (1990) 229-243.

[46] T. Vitanov, A. Popov, G. Staikov, E. Budevski, W. J. Lorenz, E. Schmidt, Slow Transformation Phenomena of Lead Adsorbates on Electrolytically Grown Ag(111) and Ag(100) Electrode Surfaces, *Electrochim. Acta*, 31 (1986) 981-989.

[47] E. Herrero, L.J. Buller, H.D. Abruña, Underpotential Deposition at Single Crystal Surfaces of Au, Pt, Ag and Other Materials, *Chemical reviews*, 101 (2001) 1897-1930.

Figure Captions

- Figure 1 SEM micrographs of Bi_{den}/Pb_{plate} (a, b, c and d) and Bi_{den}/Pb_{porous} (e, f, g, and h) at different magnifications. Top view (a through g) and cross-sectional (h) views are shown.
- Figure 2 Elucidation of Bi dendritic structure with an aberration-corrected STEM. (a, b) HAADF-STEM images showing dendritic structure at different magnifications. Note image (b) is shown after bandpass filtering. (c, d) Comparison of observed dendritic lattice arrangement with Bi rhombohedral (R-3m) model along N(100). (e) HAADF-STEM image highlighting the detailed surface-structure of the dendrite.
- Figure 3 In (a), linear sweep voltammograms of Bi-modified Pb electrodes in the CO₂-saturated 0.5 M KHCO₃ electrolyte, with Pb electrodes as the comparison. Scan rate of 5 mV s⁻¹, (b) formate faradaic efficiency (formate FE), (c) H₂ faradaic efficiency (H₂ FE), and (d) partial current density of formate ($j_{formate}$) with respect to electrolysis potential in the CO₂-saturated 0.5 M KHCO₃ electrolyte.
- Figure 4 Variation of (a) j , (b) $\log(1/R_{ct})$, and (c) C_{eff} with respect to iR -corrected potential. The data are shown for Bi_{den}/Pb_{porous} electrode in CO₂-saturated 0.5 M KHCO₃ electrolyte. The current was allowed to stabilize during 30 minutes before starting the IES measurements.
- Figure 5 Variation of (a) the current density and (b) the formate faradaic efficiency as a function of the polarization time. These measurements were performed at -0.82 V vs RHE on Bi_{den}/Pb_{porous} electrode in CO₂-saturated 0.5 M KHCO₃ electrolyte. SEM images of Bi_{den}/Pb_{porous} electrode (c) before and (d) after 15 h of CO₂ electrolysis

are shown.

Figure 6 Variation of (a) the loss of Bi EASA and (b) loss of ERC activity with the number of Pb deposition pulses. Details of the experimental procedure are giving in the text. The variation of ERC activity loss vs Bi EASA loss is depicted in (c).

Figure 7 Schematic illustration of (a) flow-cell system and (b) core of the cell. (c) Variation of the current density with the electrolysis time of Bi_{den}/Pb_{porous} electrode. See the main text for all the experimental details.

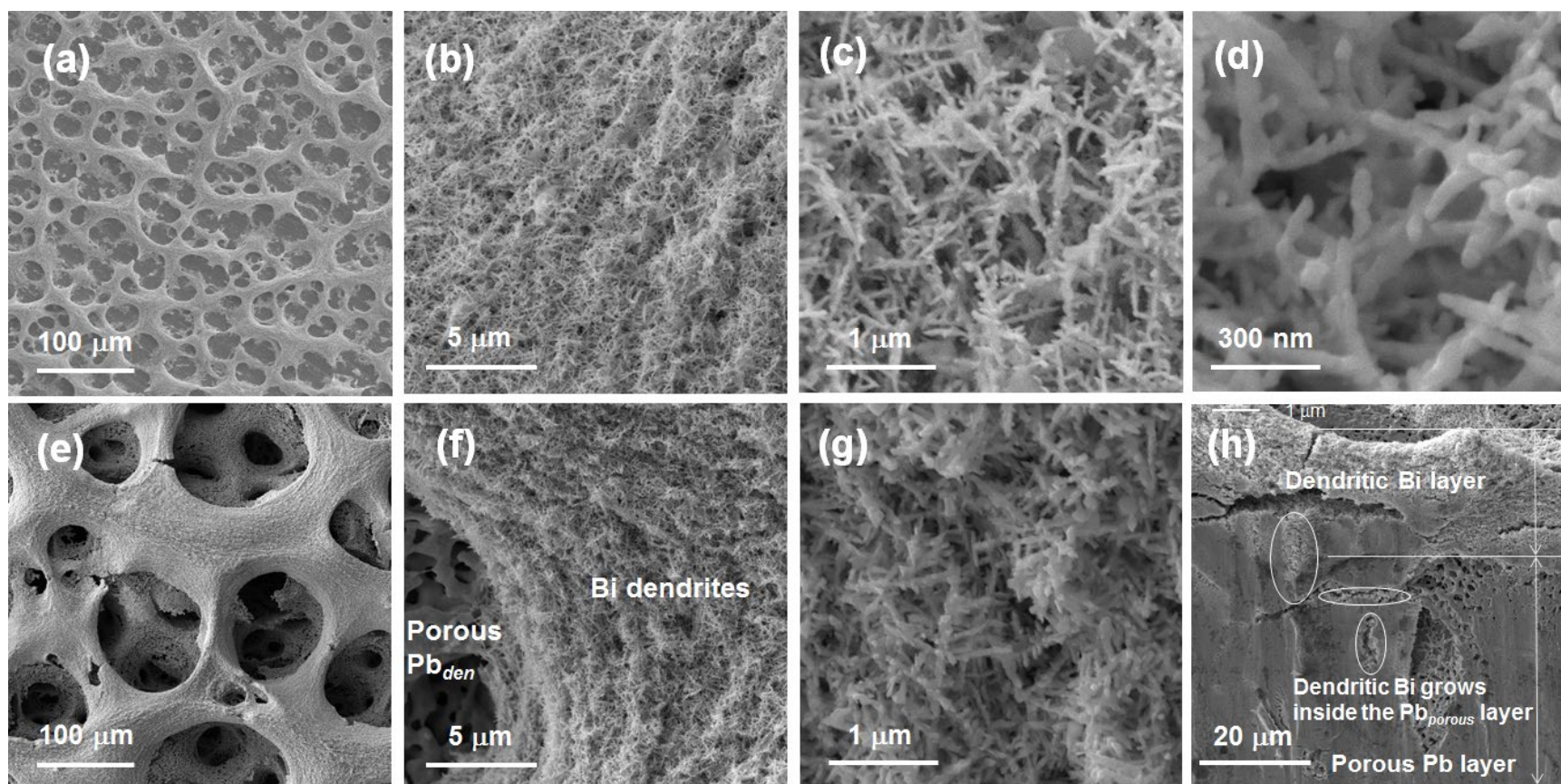


Figure 1

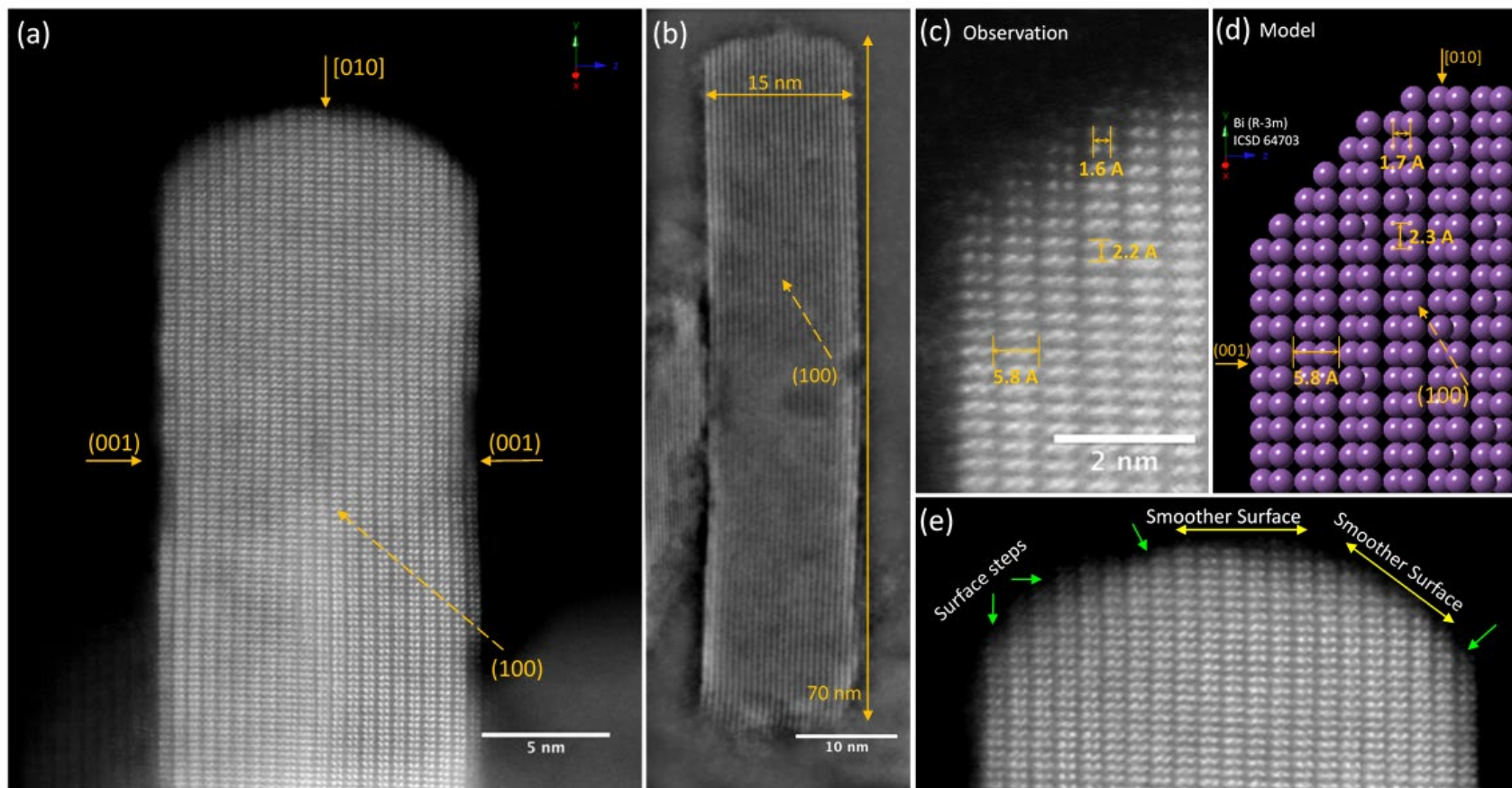


Figure 2

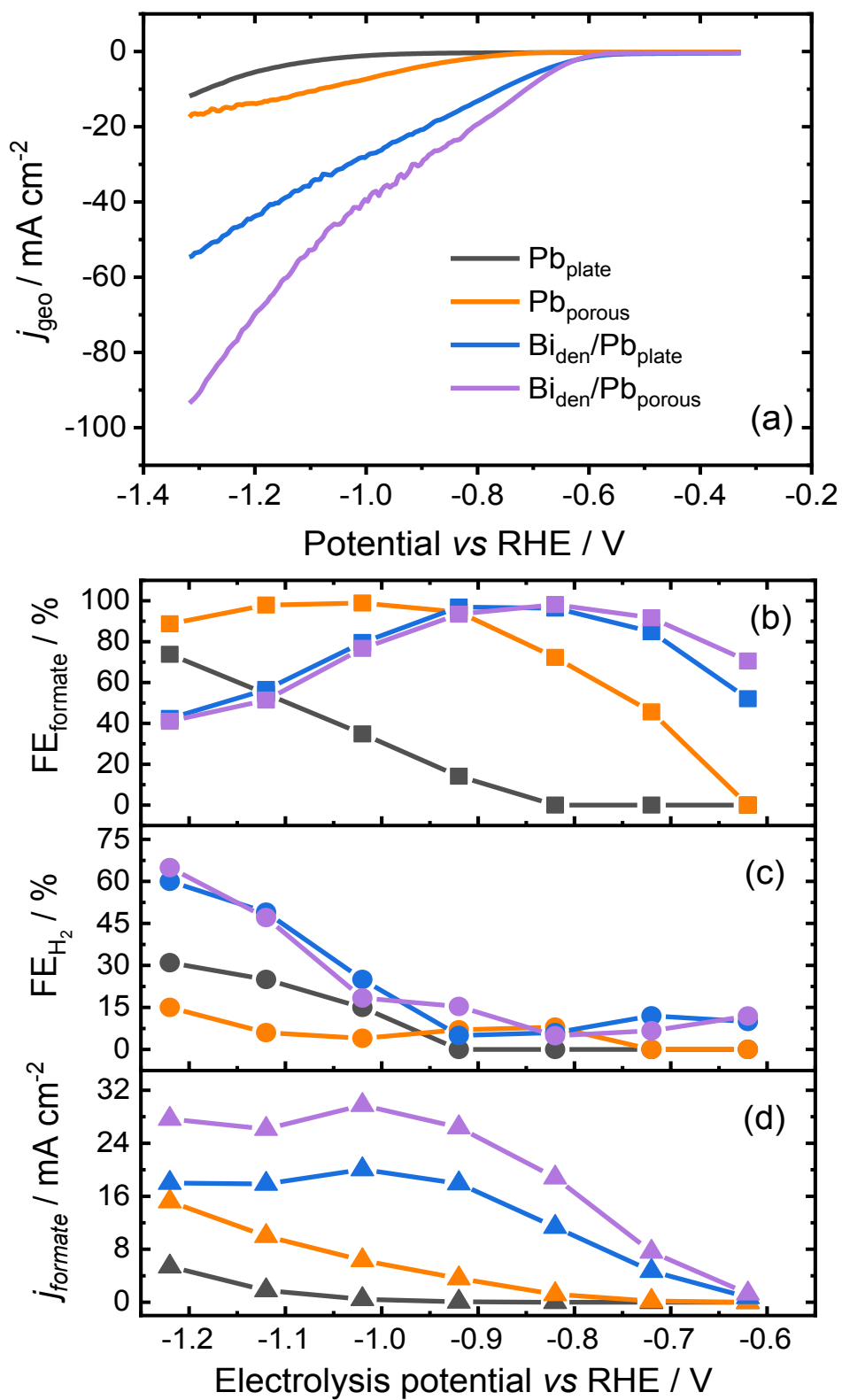


Figure 3

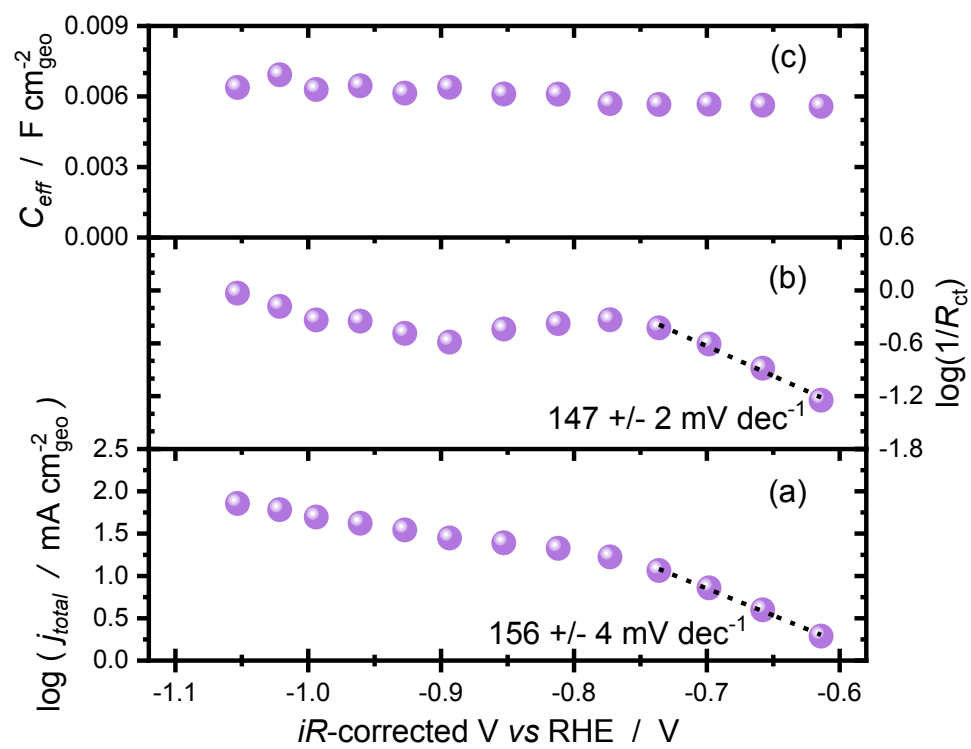


Figure 4

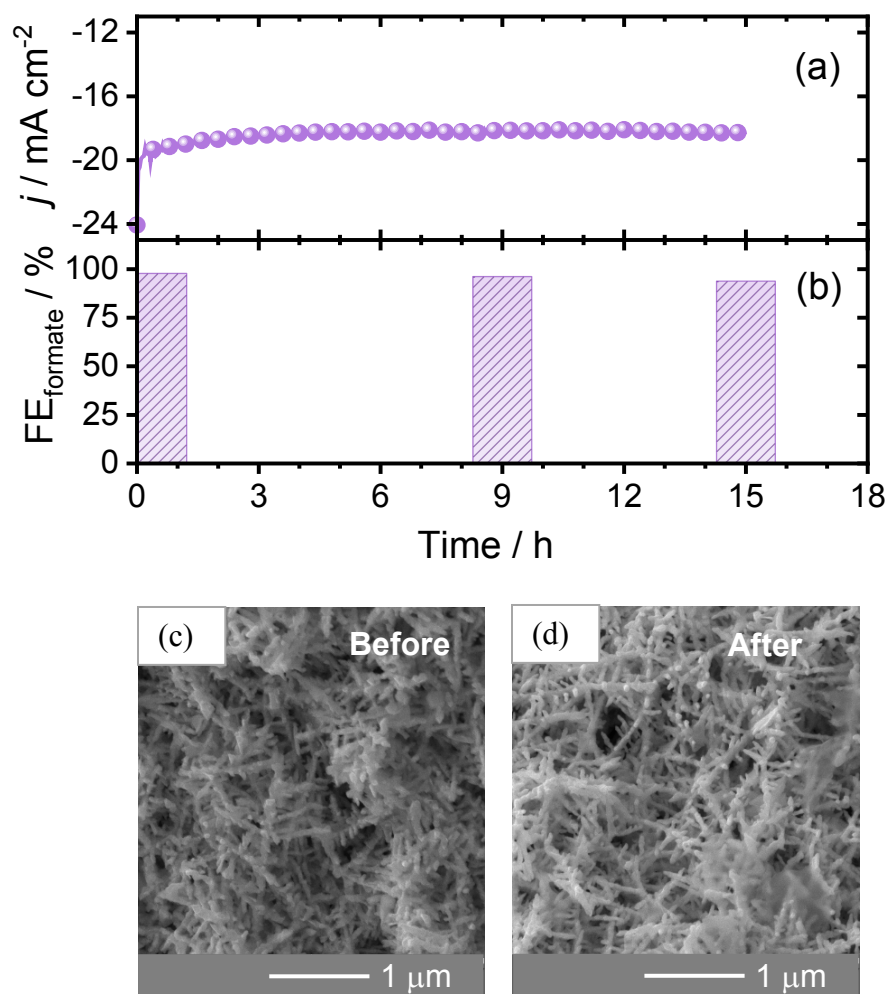


Figure 5

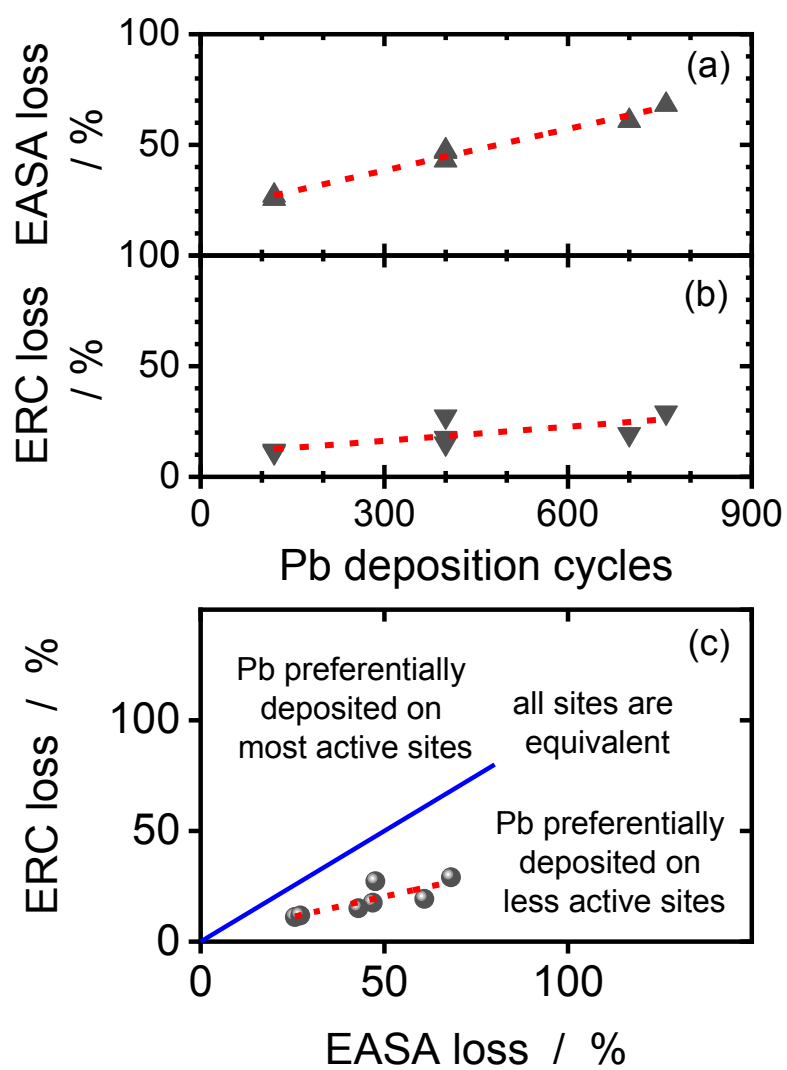


Figure 6

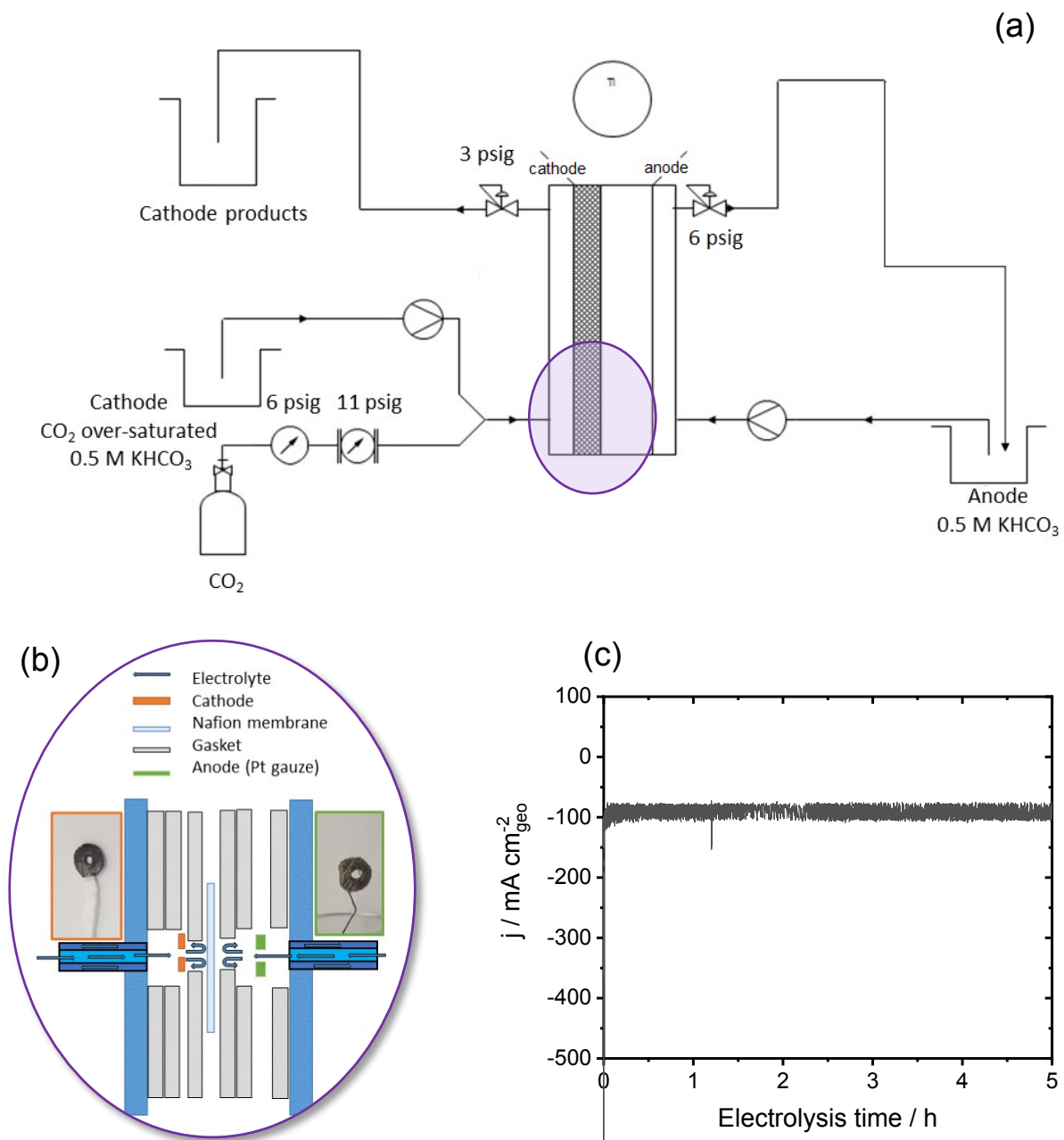


Figure 7

Supporting Information

**Uncovering the Nature of Electroactive Sites in Nano Architected Dendritic Bi for Highly
Efficient CO₂ Electroreduction to Formate**

Mengyang Fan,¹ Sagar Prabhudev,^{1,2} Sébastien Garbarino,³ Jinli Qiao,⁴
Gianluigi A. Botton,² David A. Harrington,⁵ Ana C. Tavares¹ and Daniel Guay^{1*}

SUPPLEMENTARY INFORMATION

¹ INRS-Énergie, Matériaux Télécommunications
1650 Lionel-Boulet Boulevard, P. O. Box 1020,
Varenes, QC, Canada J3X 1S2

² McMaster University, Brockhouse Institute for Materials Research and Canadian Centre
for Electron Microscopy
1280 Main Street West,
Hamilton, ON, Canada L8S 4M1

³ PRIMA Québec
505 Boulevard Maisonneuve Ouest,
Montréal, QC, Canada H3A 3C2

⁴ State Environmental Protection Engineering Center for Pollution
Treatment and Control in Textile Industry,
College of Environmental Science and Engineering, Donghua University
2999 Ren'min North Road,
Shanghai, PR China 201620

⁵ Department of Chemistry, University of Victoria
3800 Finnerty Rd, P. O. Box 1700,
Victoria, BC, Canada V8W 2Y2

* Corresponding author (guay@emt.inrs.ca)

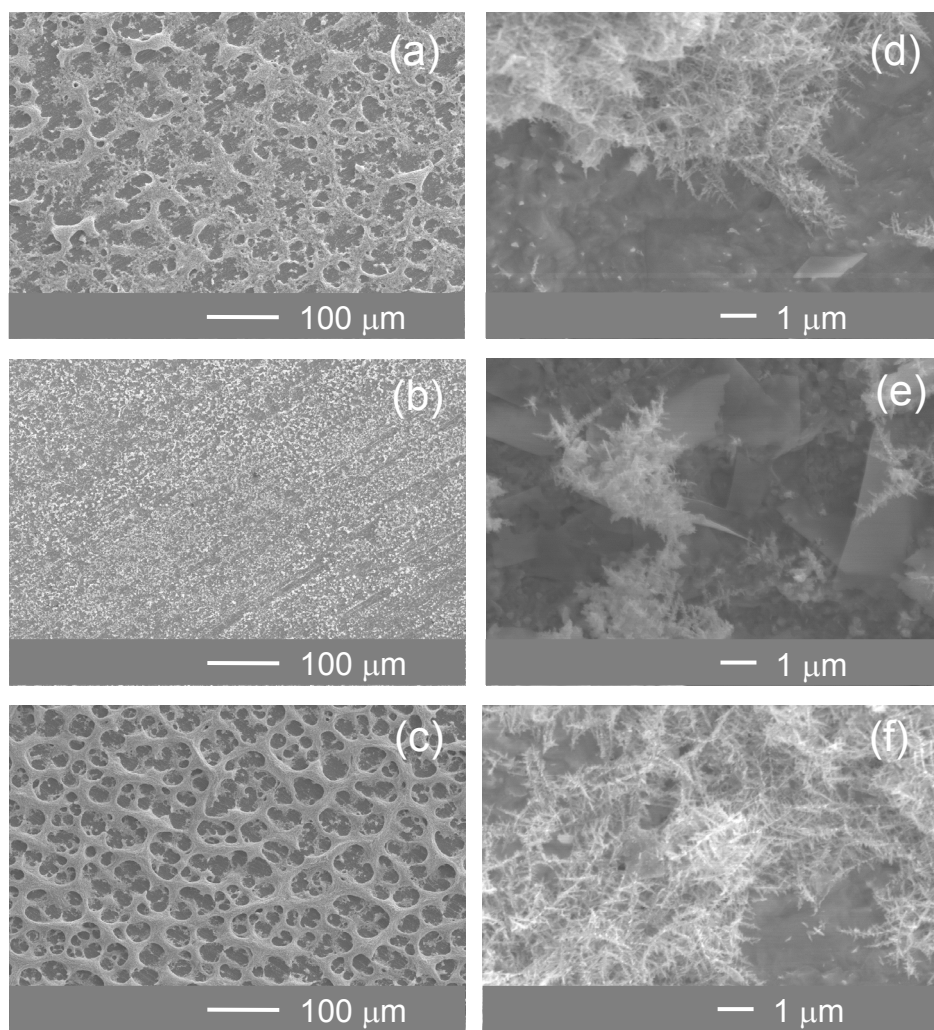


Figure S1 SEM images of Bi deposited on Pb_{plate} substrate. Deposition condition: (a, d) -0.1 A cm^{-2} , 10 min, (b, e) -0.4 A cm^{-2} , 1 min, (c, f) -0.4 A cm^{-2} , 20 min.

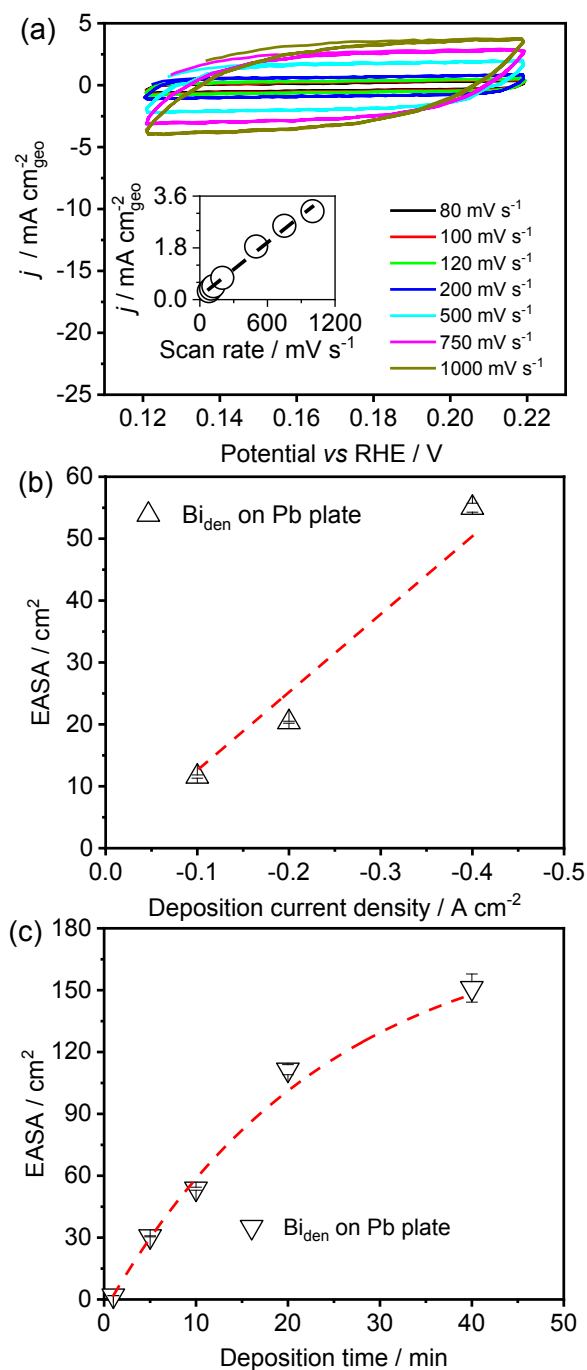


Figure S2 EASA of Bi_{den} prepared in different conditions. In (a), CVs of Bi_{den} recorded at different sweep rates in Ar-saturated 0.5 M KHCO_3 solution. The insert shows a plot of the current density recorded at 0.17 V with respect to the sweep rates. The slope of the dotted line was used to calculate the EASA by taking the value of $28 \mu\text{F cm}^{-2}$ as reference (specific charge density of

Bi).[1, 2] In (b), variation of the Bi EASA with the deposition current density (the deposition was fixed at $t_{\text{dep}} = 10$ min). In (c), variation of the Bi EASA with the deposition time (the deposition current density was fixed at -0.4 A cm^{-2}). In all cases, a Pb plate was used as substrate.

The EASA of Bi dendrites was measured by recording cyclic voltammograms (CVs) at different sweep rates in Ar-saturated 0.5 M KHCO_3 . The potential range was between 0.12 V and 0.22 V . A typical example is given in Figure S2a. Figure S2b and S2c show the EASA of Bi_{den} with respect to the deposition current density (at $t_{\text{dep}} = 10$ min) and deposition time (at $j_{\text{dep}} = -0.4 \text{ A cm}^{-2}$, respectively). The Bi EASA increases linearly with the applied deposition current. The mechanical stability of samples prepared at higher current density are poor, leading to large dispersion in their EASA. The Bi EASA increases also with the deposition time.

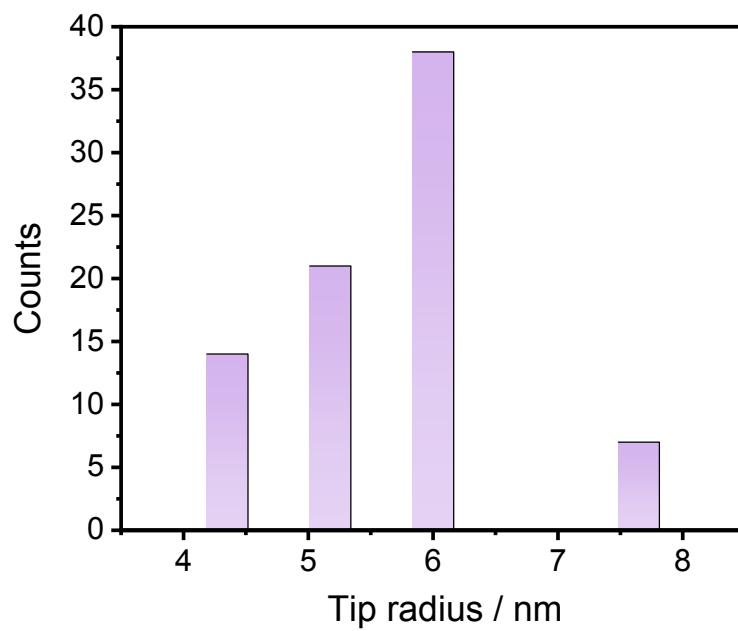


Figure S3 Histogram of tip radius obtained from measurements of 80 individual Bi nanoneedles.

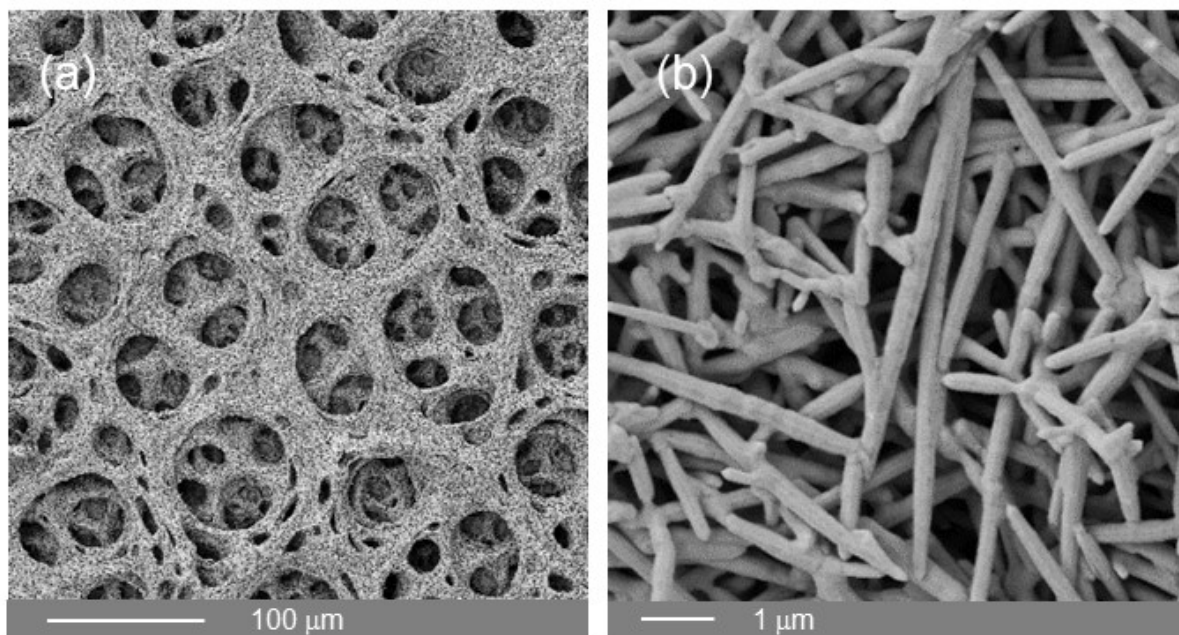
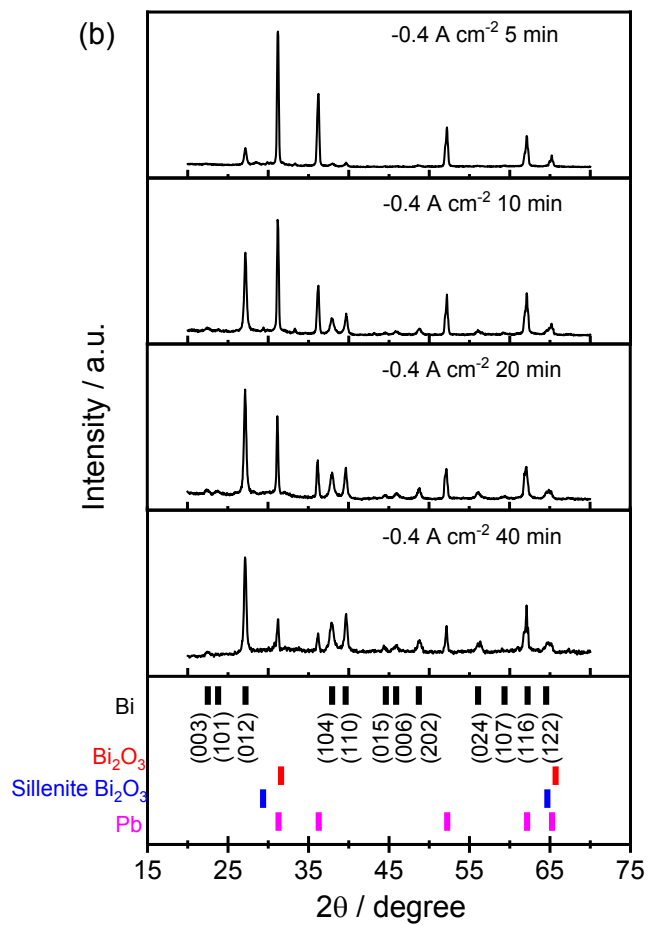
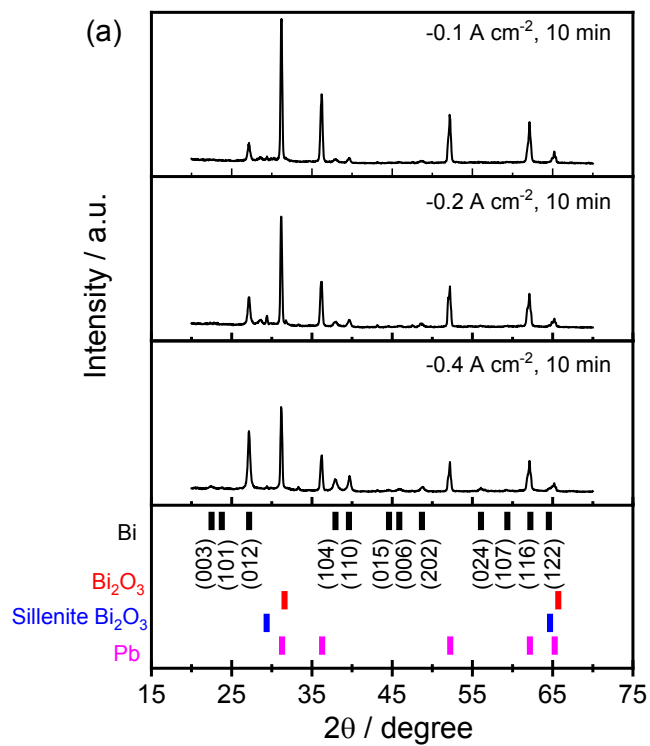


Figure S4 SEM images with various magnifications of porous Pb substrate



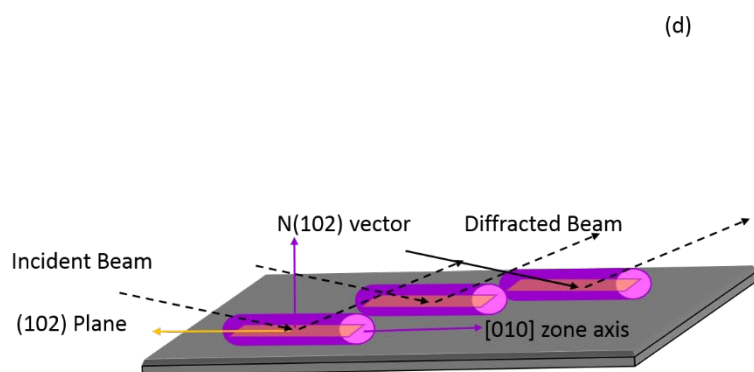
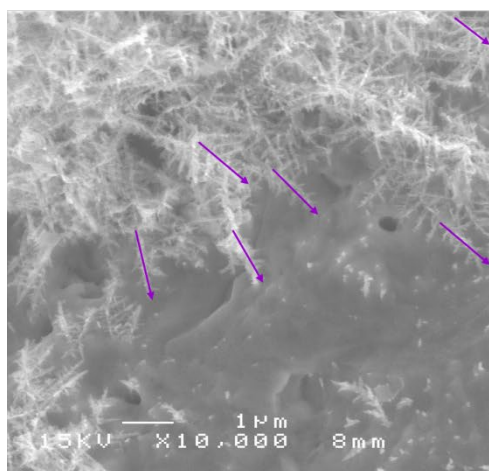
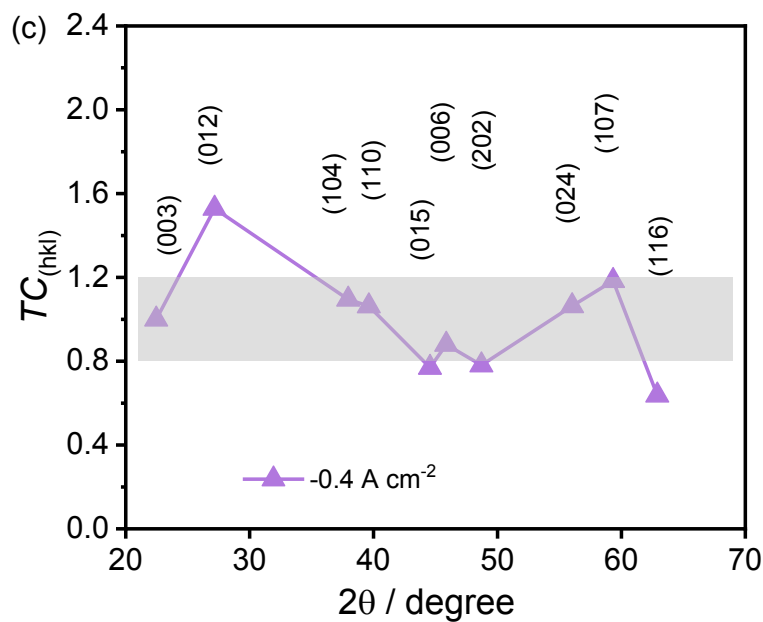


Figure S5 XRD patterns of Bi_{den} deposited at (a) different deposition current densities (with $t_{\text{dep}} = 10$ min) and (b) different deposition times (with $j_{\text{dep}} = -0.4 \text{ A cm}^{-2}$). The substrate was a Pb plate in all cases. In (c), texture coefficient, $TC_{(hkl)}$, analysis of the thicker Bi deposit. In (d), schematic representation of the growth of Bi dendrite at the surface of the substrate. The arrows indicate region where Bi grows with their $[010]$ zone axis parallel to the flat substrate.

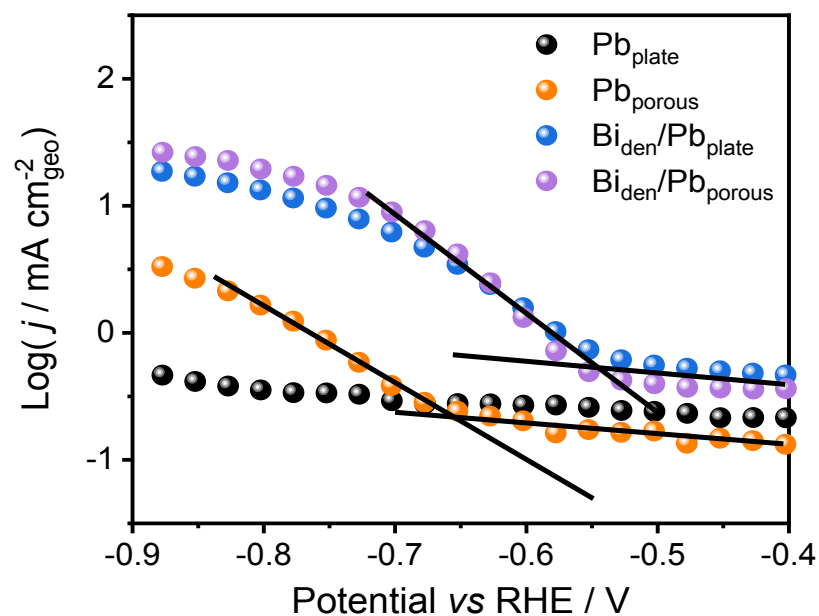


Figure S6 Linear sweep voltammograms (5 mV s^{-1}) of electrodes in CO_2 -saturated 0.5 M KHCO_3 .

The onset potential for CO_2 electroreduction was assessed by drawing $\log(-j)$ vs potential curves and taking the onset potential as the potential at which the solid lines intersect each other.

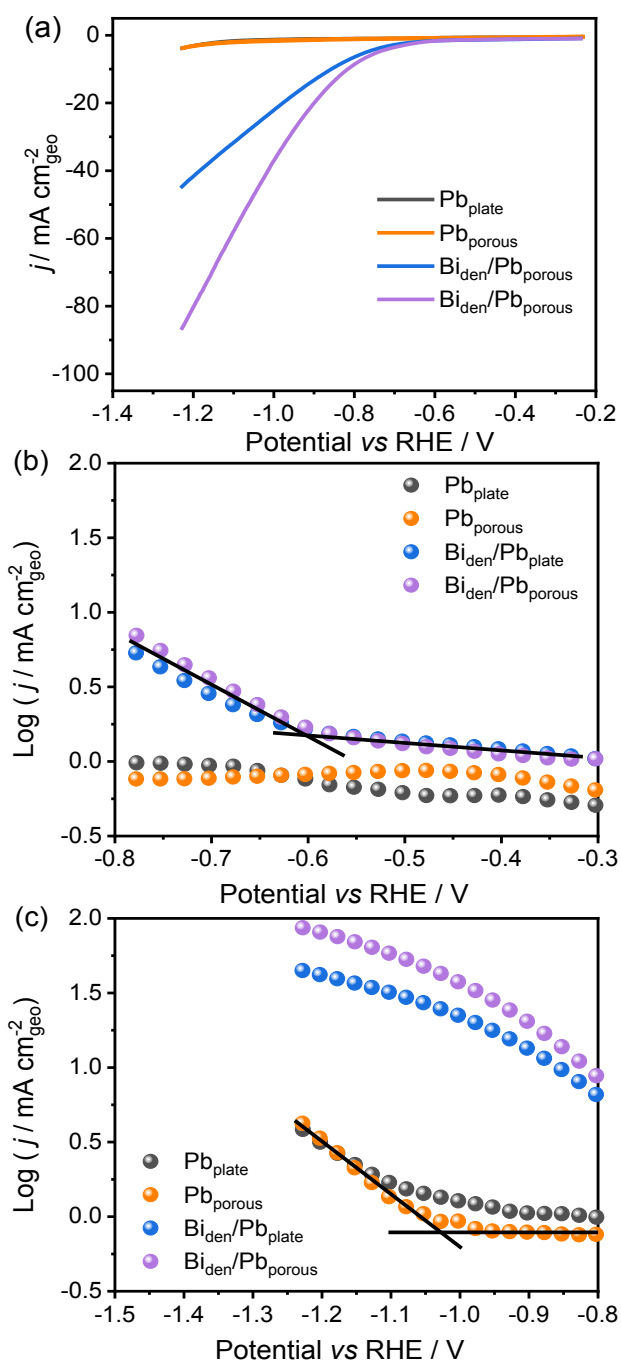


Figure S7 Linear sweep voltammograms (5 mV s^{-1}) of electrodes in Ar-saturated 0.5 M KHCO_3 .

The onset potential for H_2 electroreduction was assessed by plotting $\text{log}(-j)$ vs potential curves and taking the onset potential as the potential at which the solid lines intersect each other.

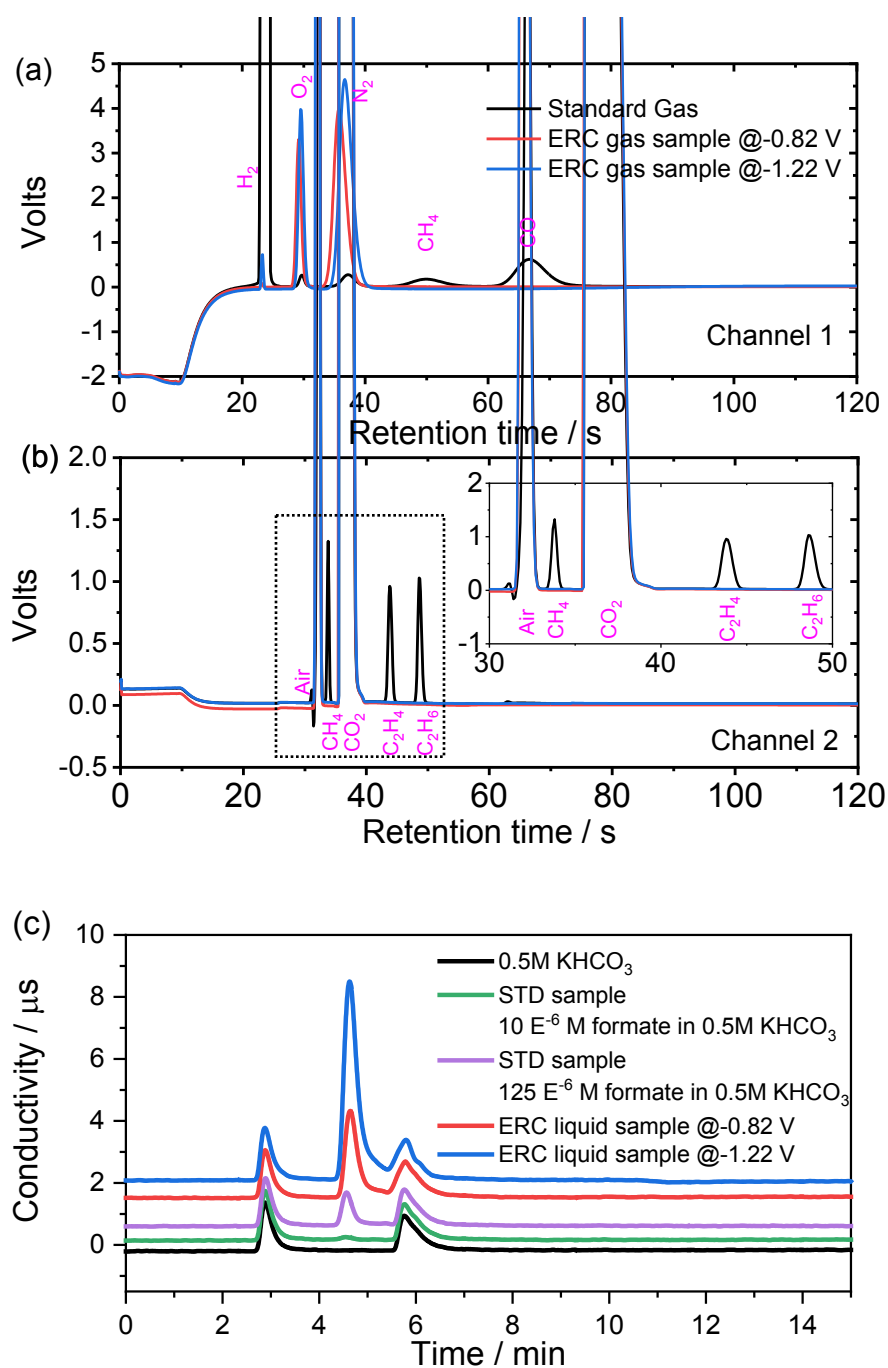


Figure S8 Typical examples of (a) GC channel 1, (b) GC channel 2, and (c) IC results. In the GC test, the standard gas sample is composed of H_2 , CO , CH_4 , C_2H_4 , C_2H_6 and CO_2 . In (a), H_2 , CH_4 , and CO are detected in channel 1. In (b), CH_4 , CO_2 , C_2H_4 , and C_2H_6 are detected in channel 2. In (c), the standard (STD) liquid sample is the formate sample dissolved in 0.5 M $KHCO_3$ solution.

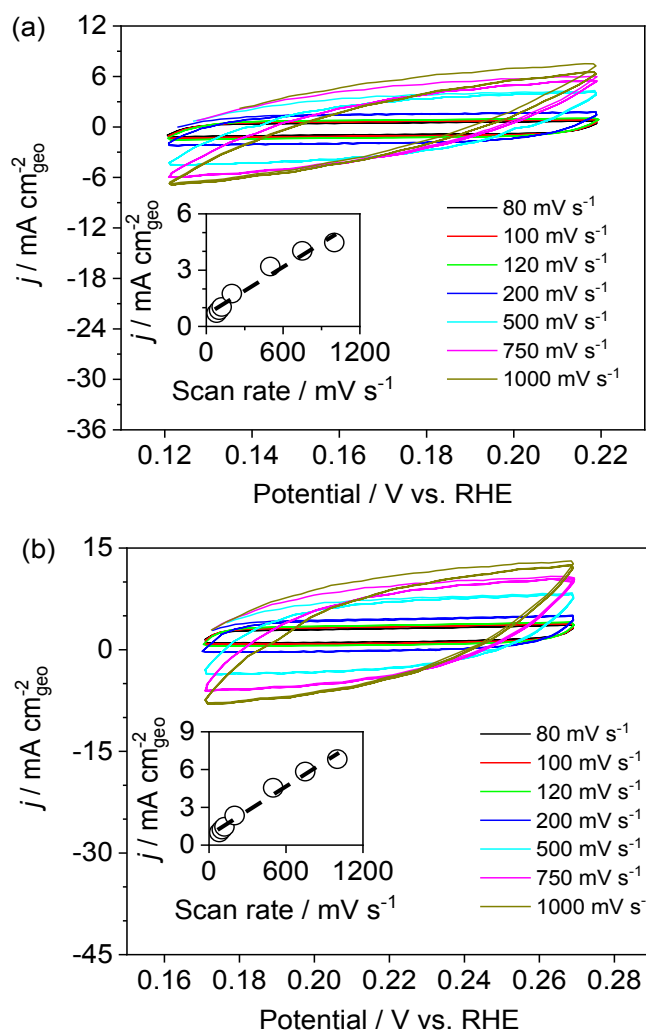


Figure S9 Determination of the Bi EASA of dendritic Bi deposited on (a) a Pb plate and (b) on a porous Pb substrate. The EASA of Bi_{den} on Pb_{plate} is 156 cm², while that of Bi_{den} on porous Pb is 231 cm².

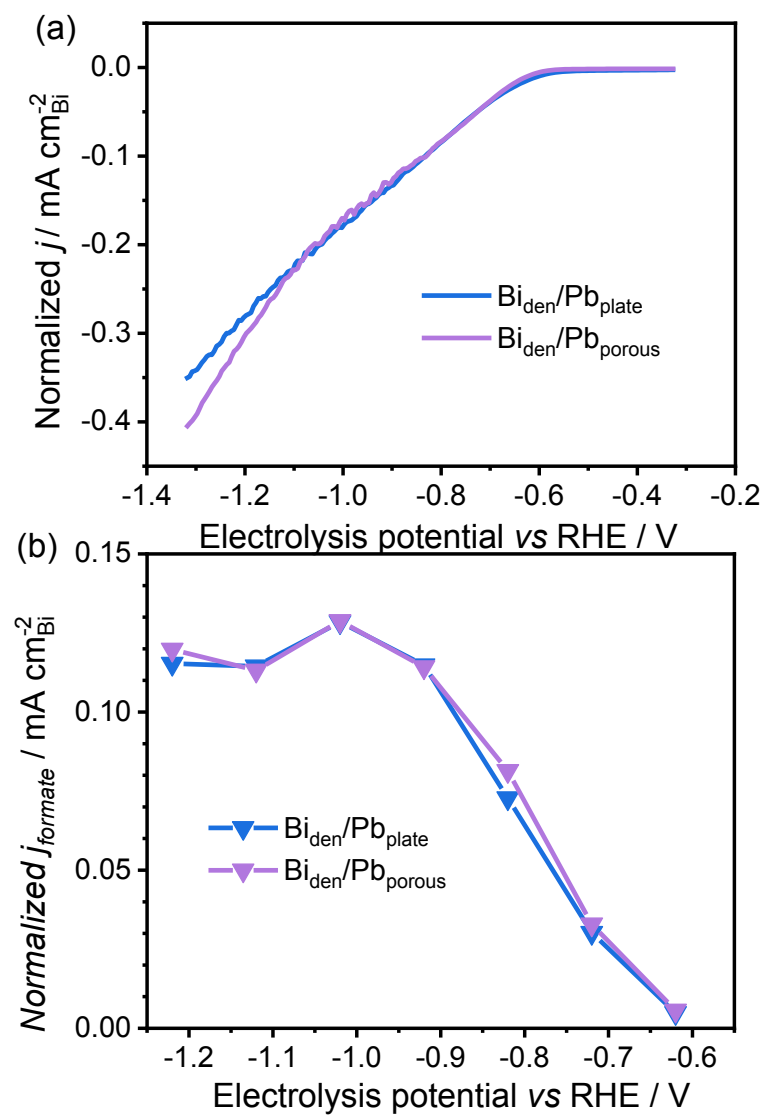


Figure S10 Bi EASA normalized (a) j and (b) j_{formate} vs. potential curves.

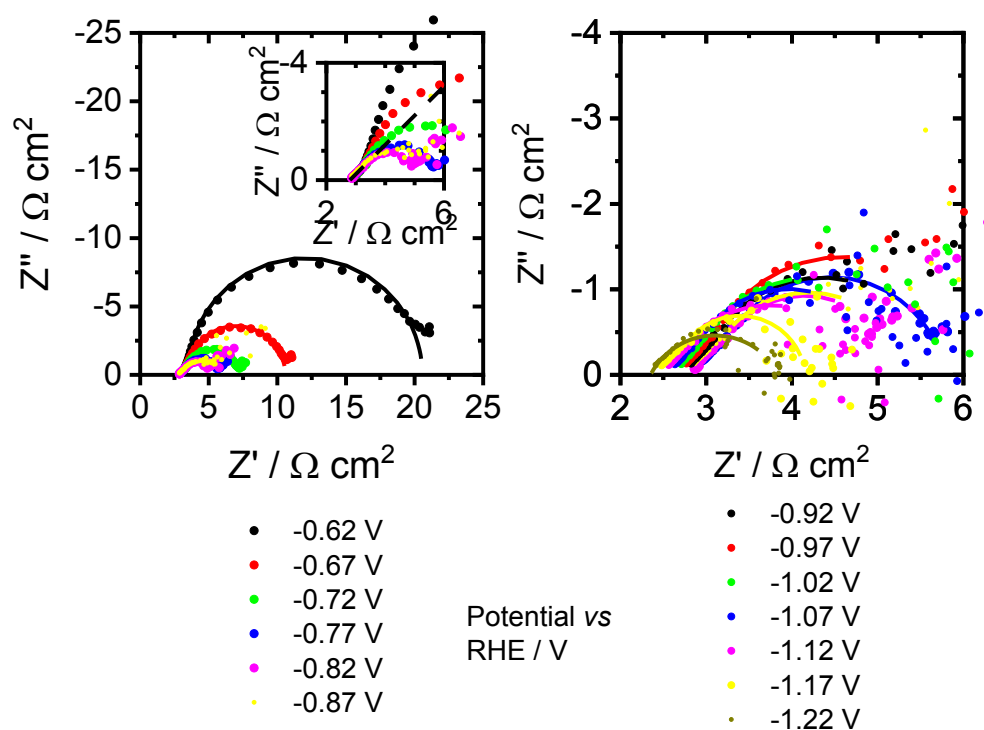
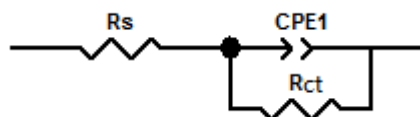


Figure S11 Nyquist plot of electrochemical impedance spectra of $\text{Bi}_{\text{den}}/\text{Pb}_{\text{porous}}$ electrodes. The applied electrode potentials were varied by steps of 0.05V from -0.62 V to -1.22 V vs. RHE. The electrolyte was CO_2 -saturated 0.5 M KHCO_3 . The experimental data (dots) and fitted curves (full lines) are shown. The data were analyzed using the following equivalent circuit:



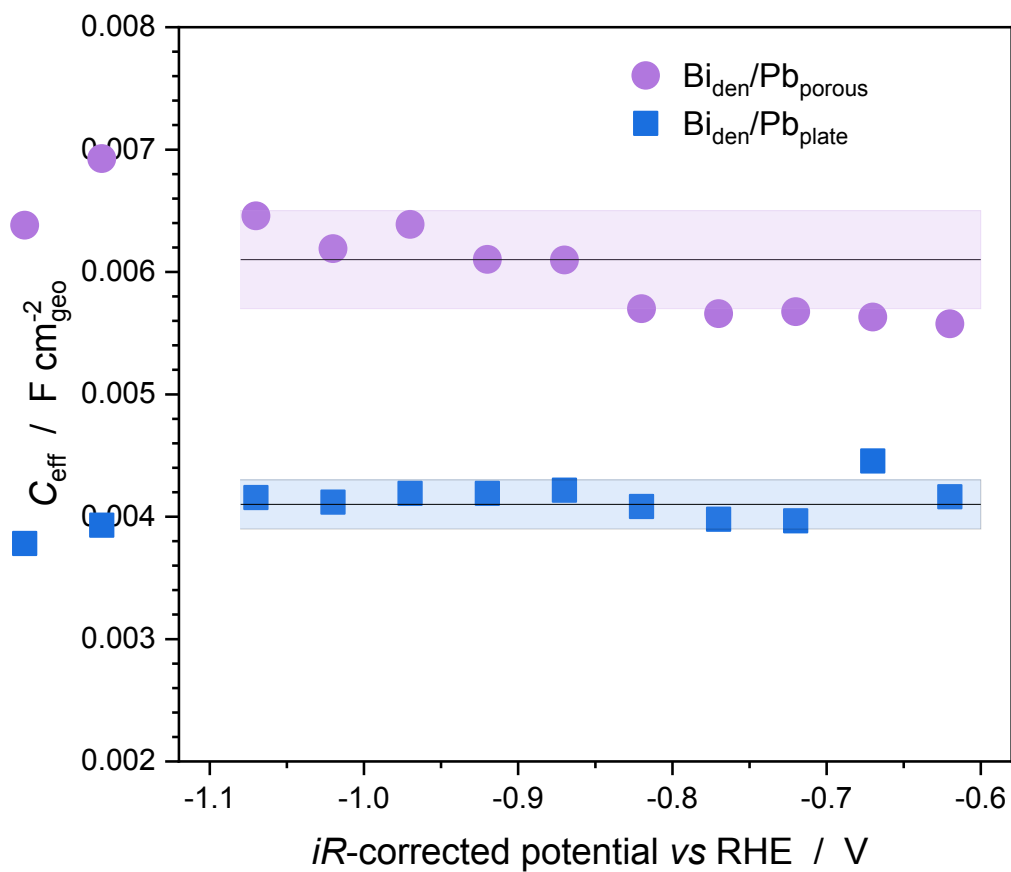


Figure S12 Variation of the effective capacitance with the iR -corrected electrode potential. The shading areas corresponds to one standard deviation.

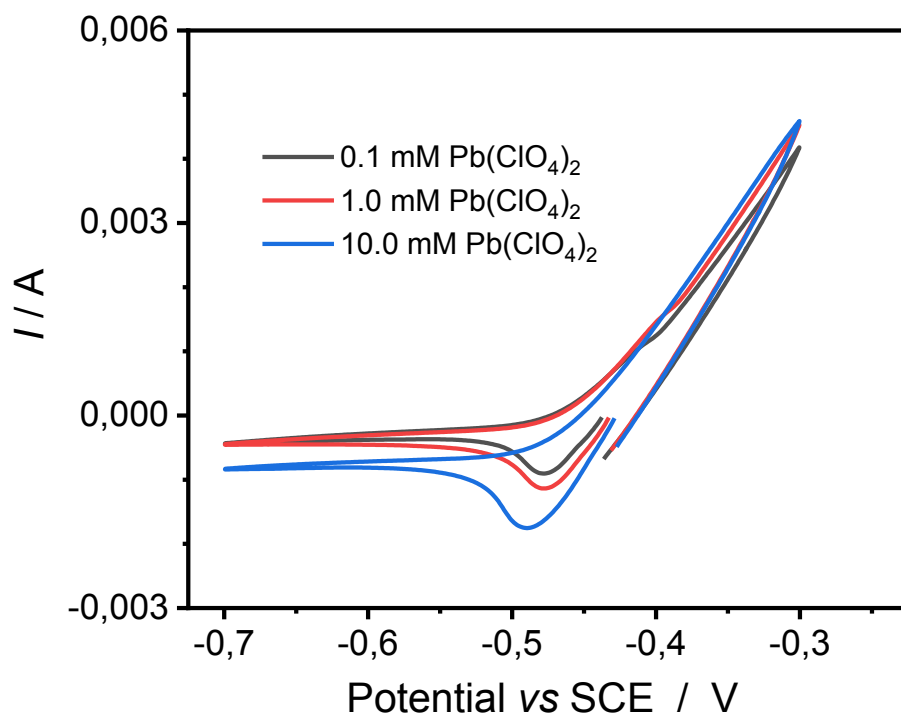


Figure S13 CV of Bi_{den}/Pb_{plate} in Pb(ClO₄)₂ + 0.1 M HClO₄ plating solution. The concentration of Pb(ClO₄)₂ was varied from 0.1 mM to 1.0 mM. The scan rate was 50 mV s⁻¹.

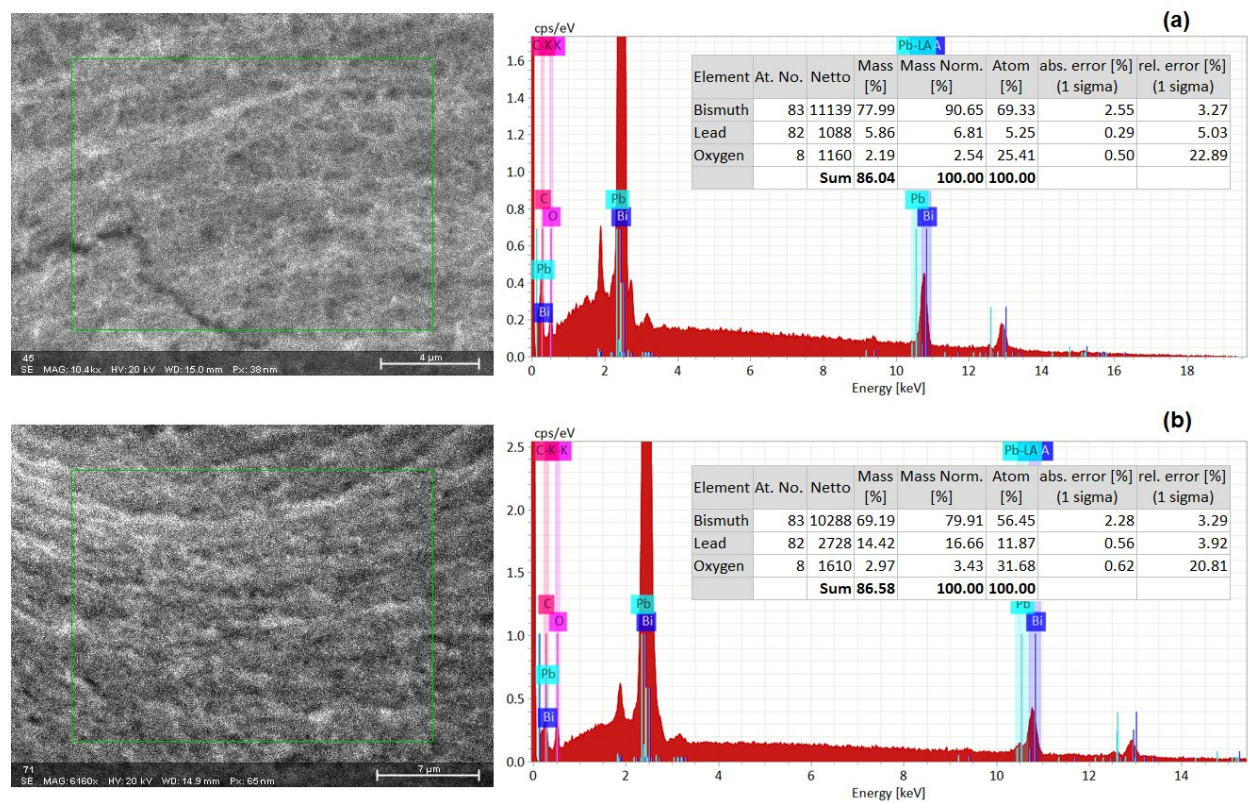
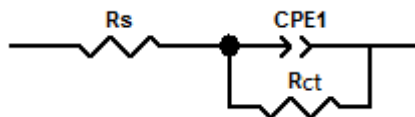


Figure S14 SEM-EDX spectrum of Bi_{den} electrode with (a) 120 cycles and (b) 400 cycles of Pb deposition.

Table S1 Fitting parameters of Bi_{iden}/Pb_{porous} electrodes at different applied electrode potentials obtained by using the following equivalent circuit. CPE1 has admittance $T(i\omega)^\phi$.



E V vs RHE	R_s ohm cm ²	R_s error	R_{ct} ohm cm ²	R_{ct} error	T mF cm ⁻² s ^{ϕ-1}	T error	ϕ	ϕ error	C_{eff} mF cm ⁻²	C_{eff} error
-0,62	3,31	0,03	17,64	0,15	7,32	0,12	0,934	0,005	5,576	0,114
-0,67	3,24	0,03	7,66	0,07	7,77	0,20	0,926	0,008	5,630	0,192
-0,72	3,21	0,03	4,06	0,05	7,89	0,25	0,928	0,009	5,675	0,233
-0,77	3,13	0,04	2,66	0,07	9,00	0,59	0,904	0,020	5,660	0,515
-0,82	3,07	0,03	2,16	0,09	9,15	0,95	0,904	0,026	5,699	0,753
-0,87	3,01	0,08	2,38	0,21	11,63	2,33	0,866	0,054	6,097	1,665
-0,92	2,96	0,05	2,75	0,17	10,82	1,47	0,879	0,036	6,103	1,089
-0,97	2,88	0,06	3,86	0,33	14,57	2,22	0,819	0,046	6,389	1,442
-1,02	2,76	0,05	3,07	0,27	14,30	2,70	0,822	0,049	6,144	1,510
-1,07	2,84	0,07	2,23	0,21	8,89	1,87	0,934	0,055	6,458	1,654
-1,12	2,67	0,16	2,16	0,30	13,43	4,27	0,845	0,097	6,298	2,293
-1,17	2,63	0,17	1,52	0,24	9,39	3,47	0,939	0,113	6,925	2,526
-1,22	2,53	0,05	1,08	0,08	6,48	1,23	0,997	0,051	6,381	1,478

The parameters R_s is the solution resistance, r_{ct} is the charge-transfer resistance and c_{eff} is the double-layer capacitance

Table S2. Comparison of CO₂ electrochemical reduction performance for dendritic Bi and recently reported Bi-cased catalysts in the literature

Electrode	Electrolyte	Potential / V vs. RHE	Formate FE / %	j_{formate} / mA cm ⁻²	Production rate* / $\mu\text{mol cm}^{-2} \text{ h}^{-1}$	Half-cell power efficiency** / %	Ref.
Bi aggregates	0.5 M KHCO ₃	-0.82	82	-0.3	5	57.1	[1]
Bi dendrites on carbon paper	0.5 M NaHCO ₃	-1.12	96	-15.0	269	58.3	[3]
Bi nanoflakes	0.1 M KHCO ₃	-0.80	100	-3.7	69	70.3	[4]
Bi dendrites	0.5 M KHCO ₃	-0.74	89	-2.7	45	64.5	[5]
Nano-Bi	0.5 M KHCO ₃	-0.92	98	-9.7	177	65.0	[6]
BiOCl nanosheets	0.5 M KHCO ₃	-0.83	92	3.7	64	63.7	[7]
Nano Bi/Cu foil	0.1 M KHCO ₃	-0.89	91	3.1	53	61.2	[8]
Micro-Bi/GDE	0.5 M KHCO ₃	-0.78	90	1.5	25	63.8	[9]
Nanoflower Bi	0.1 M KHCO ₃	-0.89	84	9.0	141	56.5	[10]
BiOx/C	0.5 M NaHCO ₃	-1.14	93	16.0	278	55.9	[11]
Bi nanosheets	0.5 M NaHCO ₃	-0.82	95	15.0~16.0	275	66.1	[12]
p-orbital delocalization-Bi	0.5 M KHCO ₃	-0.86	95	18.0	319	64.8	[13]
Pb _{den}	1 M KHCO ₃	-0.99	97	-7.5	136	62.3	[14]
Bi_{den}/ Pb_{porous}	0.5 M KHCO₃	-0.82	98	-18.8	344	68.2	This work
Bi_{den}/Pb_{porous} in flow-cell	0.5 M KHCO₃ oversaturated with CO₂	-0.82	92	95	1631	64.0	This work

* The production rate = $\text{FE}_{\text{formate}} * j / 2F$, where $\text{FE}_{\text{formate}}$ is the Faradaic Efficiency of formate, j is the steady total current density during potentiostatic CO₂ electrolysis, F is the Faraday constant.

****Half-cell power efficiency = $(1.23 - E_{\text{formate}}) * FE_{\text{formate}} / (1.23 - E_{\text{applied}})$** , where E_{formate} is 0.196 V vs. RHE, which is the thermodynamic potential of CO₂ reduction to formate, E_{applied} is the potentiostatic potential applied during CO₂ reduction. FE_{formate} is the Faradaic Efficiency of electroreduction of CO₂ towards formate. The half-cell power conversion efficiency was calculated assuming that the oxygen evolution overpotential was 0.[13]

REFERENCES

- [1] E. Bertin, S. Garbarino, C. Roy, S. Kazemi, D. Guay, Selective Electroreduction of CO₂ to Formate on Bi and Oxide-derived Bi Films, *J. CO₂ UTIL.*, 19 (2017) 276-283.
- [2] V. Ivaništšev, R.R. Nazmutdinov, E. Lust, Density Functional Theory Study of the Water Adsorption at Bi(111) Electrode Surface, *Surf. Sci.*, 604 (2010) 1919-1927.
- [3] H. Zhong, Y. Qiu, T. Zhang, X. Li, H. Zhang, X. Chen, Bismuth Nanodendrites as a High Performance Electrocatalyst for Selective Conversion of CO₂ to Formate, *J. Mater. Chem. A*, 4 (2016) 13746-13753.
- [4] S. Kim, W.J. Dong, S. Gim, W. Sohn, J.Y. Park, C.J. Yoo, H.W. Jang, J.-L. Lee, Shape-controlled Bismuth Nanoflakes as Highly Selective Catalysts for Electrochemical Carbon Dioxide Reduction to Formate, *Nano Energy*, 39 (2017) 44-52.
- [5] J.H. Koh, D.H. Won, T. Eom, N.-K. Kim, K.D. Jung, H. Kim, Y.J. Hwang, B.K. Min, Facile CO₂ Electro-Reduction to Formate via Oxygen Bidentate Intermediate Stabilized by High-Index Planes of Bi Dendrite Catalyst, *ACS Catal.*, 7 (2017) 5071-5077.
- [6] Y. Qiu, J. Du, W. Dong, C. Dai, C. Tao, Selective Conversion of CO₂ to Formate on a Size Tunable Nano-Bi Electrocatalyst, *J. CO₂ UTIL.*, 20 (2017) 328-335.
- [7] H. Zhang, Y. Ma, F. Quan, J. Huang, F. Jia, L. Zhang, Selective electro-reduction of CO₂ to formate on nanostructured Bi from reduction of BiOCl nanosheets, *Electrochem. Commun.*, 46 (2014) 63-66.
- [8] W. Lv, J. Zhou, J. Bei, R. Zhang, L. Wang, Q. Xu, W. Wang, Electrodeposition of nano-sized bismuth on copper foil as electrocatalyst for reduction of CO₂ to formate, *Appl. Surf. Sci.*, 393 (2017) 191-196.

- [9] X. Zhang, T. Lei, Y. Liu, J. Qiao, Enhancing CO₂ electrolysis to formate on facilely synthesized Bi catalysts at low overpotential, *Appl. Catal. B-Environ.*, 218 (2017) 46-50.
- [10] J. Bei, R. Zhang, Z. Chen, W. Lv, W. Wang, Efficient Reduction of CO₂ to Formate Using in Situ Prepared Nano-Sized Bi Electrocatalyst, *International Journal of Electrochemical Science*, (2017) 2365-2375.
- [11] C.W. Lee, J.S. Hong, K.D. Yang, K. Jin, J.H. Lee, H.-Y. Ahn, H. Seo, N.-E. Sung, K.T. Nam, Selective Electrochemical Production of Formate from Carbon Dioxide with Bismuth-Based Catalysts in an Aqueous Electrolyte, *ACS Catal.*, 8 (2018) 931-937.
- [12] N. Han, Y. Wang, H. Yang, J. Deng, J. Wu, Y. Li, Y. Li, Ultrathin Bismuth Nanosheets from In Situ Topotactic Transformation for Selective Electrocatalytic CO₂ Reduction to Formate, *Nat. Commun.*, 9 (2018) 1320.
- [13] S. He, F. Ni, Y. Ji, L. Wang, Y. Wen, H. Bai, G. Liu, Y. Zhang, Y. Li, B. Zhang, H. Peng, The p-Orbital Delocalization of Main-Group Metals to Boost CO₂ Electroreduction, *Angew. Chem. Int. Ed. Engl.*, 57 (2018) 16114-16119.
- [14] M. Fan, S. Garbarino, G.A. Botton, A.C. Tavares, D. Guay, Selective Electroreduction of CO₂ to Formate on 3D [100] Pb Dendrites with Nanometer-sized Needle-like Tips, *J. Mater. Chem. A*, 5 (2017) 20747-20756.